Nanopipettes as a Tool to Study Single Biological Entities

Anna Rose Leach

Submitted in accordance with the requirements for the degree of *Master of Philosophy*

The University of Leeds

School of Electronic and Electrical Engineering

October 2022

Declaration

The candidate confirms that the work submitted is her own, except where work which has formed part of jointly authored publications has been included. The contribution of the candidate and the other authors to this work has been explicitly indicated below. The candidate confirms that appropriate credit has been given within the thesis where reference has been made to the work of others.

Chapter 5 contains materials published by the candidate and co–authors M. Raveendran, T. Hopes, J.L. Aspden and P. Actis, where M. Raveendran and the candidate were joint first authors. Preliminary translocation studies, analysis, hypotheses and conclusions were generated by the candidate, which were further validated by M. Raveendran in the experiments and statistical analysis presented in the paper. The ribosomes and polysomes used were prepared by T. Hopes from J.L Aspden's group. P. Actis is the candidate's primary supervisor.

Publication: Raveendran, M., Leach, A.R., Hopes, T., Aspden, J.L. and Actis, P., 2020. Ribosome fingerprinting with a solid-state nanopore. ACS sensors, 5(11), pp.3533-3539.

Acknowledgements

I wish to express my deepest gratitude to Dr. Paolo Actis, who has provided continued academic, practical and emotional support throughout the duration of this project. I would like to thank him for giving me this opportunity, for believing in me, for guiding me and for always having time for me. Most of all, I would like to thank him for always wanting the best for me, and supporting me with any endeavour I have undertaken.

I would like to thank the Pollard Institute as a whole for their support. In particular I extend my gratitude to Chalmers for having provided me with samples, helping me troubleshoot and giving me inspiration. Furthermore, I would like to express my gratitude to Tayah Hopes for providing me with my ribosome and polysome samples, and to Julie Aspden for making the collaboration possible. I additionally would like to thank Siu Lee for providing my viral RNA samples, and to Prof. Mark Harris for enabling this project.

Finally, and above all, I would like to thank my friends and family for their continued support. To my partner, Brad, thank you for always standing by me and for all of your love and support, you are my rock. And to my parents, thank you for your encouragement and for your love and support, including financial, throughout the course of this project, without you none of this would be possible. Thank you for making my education possible and for giving me strength when things were difficult.

Dedication

To my Dad, for igniting and nurturing my interest in science, for always being interested in my work and for being my role model. Your mind-set, outlook and values are a constant source of inspiration to me. Thank you for teaching me what is truly important in life- each day I try to cultivate the peace, kindness and patience that come so naturally to you.

Abstract

Nanopores offer a fast, convenient label-free platform for the detection and analysis of single biological entities, revealing data unseen in bulk analysis due to averaging. The ribosome is a biological entity of particular interest, due to its key role in protein synthesis. However, one challenge associated with this macromolecule is their typical small sample size, particularly when one is selecting ribosomes from specific tissues, or time points in development. Here, a nanopipette platform for single ribosome analysis is reported, enabling the fingerprinting of 80S ribosomes and polysomes from *Drosophila melanogaster* cultured cells and ovaries. When the nanopipette is filled with a solution containing the ribosome or polysome sample of interest, an application of a positive voltage to the nanopipette electrode causes the translocation of the macromolecules across the nanopipette pore. Within this thesis, it is demonstrated that the peak amplitude of 80S ribosomes is significantly different to those of polysomes, and can be used to distinguish them in a mixed isolate. Furthermore, it is reported within this work that the nanopipette platform can be used to distinguish large polysomes from smaller polysomes, and as large polysomes represent mRNAs which are being actively translated, this is of great biological significance. Moreover, this thesis demonstrates the successful detection of a Chikungunya virus (CHIKV) RNA replicon, which will enable future work for the injection of viral genomes into living cells.

Contents

List of Figures

List of Tables

Abbreviations

ATP	Adenosine Phosphate
cDNA	Copy DNA
CHIKV	Chikungunya virus
CIP	Calf intestinal alkaline phosphatase
ClyA	Cytolysin A
DEPC	Diethyl pyrocarbonate
DNA	Deoxyribonucleic acid
EDL	Electrical Double Layer
EDTA	Ethylenediaminetetraacetic acid
EM	Electron Microscopy
FIB	Focussed ion beam
GFP	Green fluorescent protein
IHP	Inner Helmholtz Plane
MOPS	3-(N-morpholino)propanesulfonic acid
mRNA	Messenger ribonucleic acid
MspA	*Mycobacterium smegmatis* porin A
MW	Molecular Weight
OHP	Outer Helmholtz Plane
OmpG	Outer membrane protein G
ORF	Open reading frame
PBS	Phosphate-buffered saline
PEG	Poly(ethylene) glycol
qRT-PCR	Quantitative reverse transcription polymerase chain reaction
RNA	Ribonucleic acid
rRNA	Ribosomal ribonucleic acid
SA	Streptavidin
SEM	Scanning electron microscope
SICM	Scanning Ion Conductance Microscope
SNR	Signal-to-noise ratio
sm(ORF)	Small open reading frames
TE	Tris-EDTA
TEM	Transmission electron microscope

tRNA	Transfer ribonucleic acid
UV	Ultraviolet

Chapter 1- Introduction to Nanopores and Nanopipettes

1.1 Nanopores and Resistive Pulse Sensing

Nanopores offer a simple, label-free method of profiling single molecules, a powerful technique revealing heterogeneity which is normally unseen in bulk analysis due to averaging. As only small amounts of analyte are necessary, both in volume and concentration, nanopores are able to detect and analyse scarce and/or costly samples where only a small quantity is available [6, 7]. Nanopores employ a technique called resistive pulse sensing [8-14], based on the Coulter counter which was developed in the 1950s to count cells [15]. Here, two chambers of electrolyte were connected by an aperture. A voltage is applied across the aperture, causing the cells to pass through the pore. As the cell passes from one side of the pore to the other, it temporarily blocks the flow of ions, resulting in a reduction in the ionic current (resistive-pulse). The principle of the Coulter counter has seen a resurgence in popularity over the past 30 years, with the pore size being shrunk to the nanoscale to allow the detection of single molecules. The size and shape of the current blockade generated by the molecule can then be used to give valuable information about the analyte, such as size, conformation, structure and charge, and the frequency of current modulations reflects the sample concentration [8-14].

A nanopore consists of a membrane between two electrolyte baths, with a nanometer sized hole connecting the two, which should be comparable to the size of the analyte being detected. The electrolyte solution at either side of the membrane each contain an electrode, and when a potential difference is applied across them, an ionic current will flow through the pore [2-4]. There are two main classes of nanopore, biological and solid-state. Biological nanopores are usually transmembrane proteins from bacteria, such as α-hemolysin from *Staphylococcus aureus* and Cytolysin A (ClyA) from *Escherichia coli* [1, 3], whereas solid-state nanopores are usually fabricated from artificial membranes made from, for example, silica, with an ion or electron beam used to drill nanoscale holes [4]. Another type of solid-state nanopore is a nanopipette. Nanopipettes are glass pipettes with a nanoscale tip, usually fabricated for borosilicate or quartz capillaries, the latter being used for nanopipettes with

smaller pore sizes, due to its higher melting point [16]. The different classes of nanopore and an illustration of a nanopore experiment are shown within Box 1.1.

Box 1.1: A Nanopore Experiment

The different types of nanopore, biological, solid state and nanopipette, are shown in Figure 1.1(a). In a nanopore experiment, illustrated in Figure 1.1(b), a membrane separates two electrolyte baths, with a nanopore in the centre of the membrane being the only point of connection between the two chambers. Within each chamber, there is an electrode, and when a constant voltage is applied between the two electrodes, an ionic current flows through the nanopore from one chamber to another, at a constant, baseline rate. However, if one side of the membrane is filled with a mixture of the electrolyte and a molecule of interest, it will pass across the nanopore, either by electrophoresis or electroosmosis, and the ion flow is constricted and the current drops temporarily. This is detected as a current blockade, or peak. The amplitude of the peak resembles the amount of current blocked by the molecule (peak amplitude, ΔI), its width demonstrates the length of time the molecule took to cross the pore (dwell time, δt), and the area underneath the peak gives the charge. By analysing the characteristics of the peak, we can gather information on the molecule, for example its size, charge and structure. Furthermore, an ion current signature can be generated for individual molecules, and therefore can be used to distinguish different molecules in solution. [1-4]

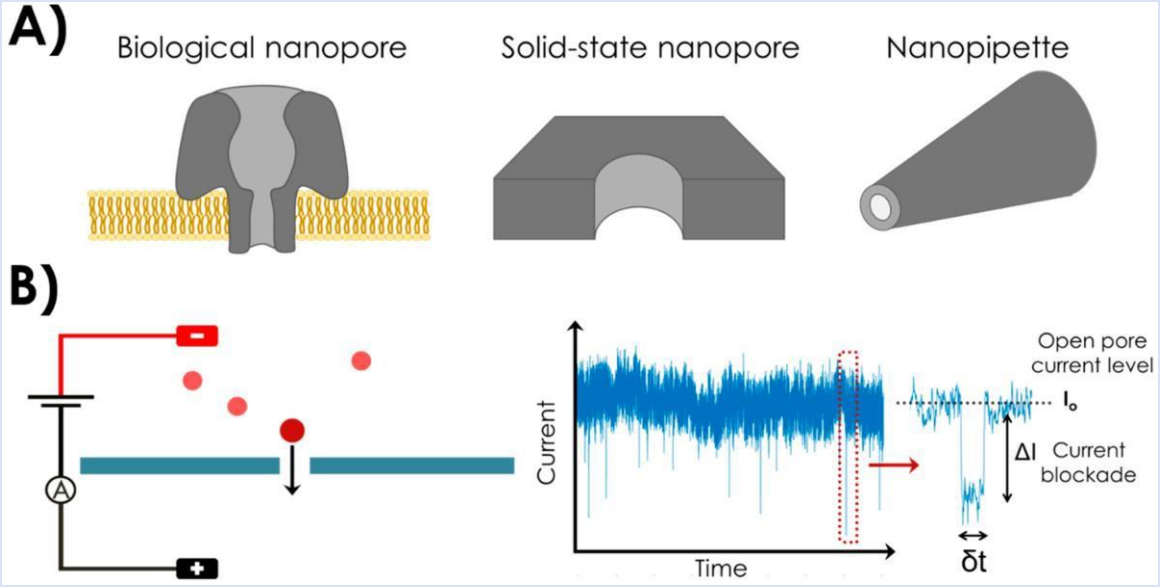

Figure 1.1 Image taken from [1] (a) The different classes of nanopore sensors. (a) A biological nanopore embedded within a lipid membrane, a solid state nanopore and a nanopipette. (b) A schematic of a typical nanopore experiment (left). Two chambers either side of the nanopore are both fitted with electrodes, and are filled with electrolyte solution. Molecules of interest inside the electrolyte solution in one chamber pass through the nanopore when a voltage is applied between the two electrodes. A typical ion current trace for a nanopipette experiment (right), the zoomed in panel showing each current modulation is a peak with an amplitude and dwell time that can be measured and recorded.

In a seminal paper in 1996 [17], Kasianowicz *et al*. demonstrated the translocation of individual single strands of deoxyribonucleic acid (DNA) and ribonucleic acid (RNA) through an α-hemolysin pore from *S. aureus*, finding that the dwell time of each current blockade event corresponded to the length of nucleic acid chain. The authors hypothesised that because the pore could detect the lengths of the strands of nucleic acid, that in the future nanopores could be able to detect the molecular differences between individual nucleotides, and thus be used to sequence nucleic acid [17]. This experiment formed the foundation for the Oxford Nanopore technology, a commercially available, portable nanopore sequencer which has been employed in numerous next-generation sequencing studies to-date [18-21]. Whilst DNA sequencing has been the main focus of nanopore experiments in the past, there exists a large potential of nanopores to study single biological molecules and structures beyond nucleic acids, such as proteins [22, 23] and metabolites [2, 24, 25].

1.2 Types of Nanopore

1.2.1 Biological Nanopores

Biological nanopores are transmembrane proteins which mediate the transport of molecules from one side of a biological membrane to another. There are two main types of biological nanopores: toxins, which form a pore to induce cell lysis by damaging the osmotic balance of a cell, for example α-hemolysin (1.4 nm at its narrowest), and membrane channels, such as *Mycobacterium smegmatis* porin A, MspA (inner diameter 1.2 nm) and Outer Membrane Protein G, OmpG (1.3 nm) [1, 26]. Biological nanopores can easily be engineered, using site-directed mutagenesis [3].

One of the most commonly utilised biological nanopores is α-hemolysin, which is a toxin produced by *S. aureus.* It is a heptameric transmembrane protein which assembles in a mushroom shape, and has an opening at the cap, leading to a vestibule, which is in turn connected to a β-barrel transmembrane region (Figure 1.2). The narrowest region of the pore is where the vestibule meets the transmembrane β-barrel stem, which has an opening of 1.4

nm in diameter [3, 27]. α- hemolysin is important for DNA-translocation studies, as it produces results which are extremely reliable [1]. However, due to its small diameter, it is only suitable for translocation of single-stranded DNA, as double stranded DNA is too large to traverse the pore [27]. α-hemolysin is a highly stable biological nanopore, and stays open when exposed to various different experimental conditions, such as temperatures up to 90°C [10, 27]

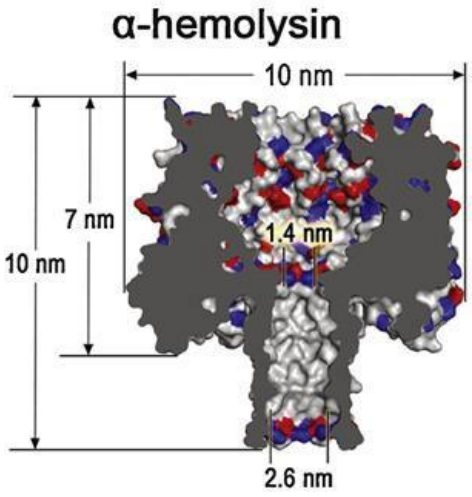

Figure 1.2 The structure of α-hemolysin, showing a cap opening at the top, leading into a vestibule, which is connected to a β-barrel stem by an aperture of 1.4 nm. Source: Adapted from [3].

Other, larger biological nanopores include ClyA, which has an inner diameter of 3.3 nm, and phi29 motor pores with internal diameter of 3.6 nm. These nanopores are useful for analysing larger biomolecules such as peptides and small proteins [1, 3].

Because the pore sizes and conformations of biological nanopores are consistent and precise, the signals produced by translocation events are extremely reproducible between experiments [1]. Additionally, their naturally occurring small pore sizes enable a high degree of sensitivity which can enable the resolution of individual bases in DNA, with Oxford Nanopore employing biological nanopores in their commercially available nanopore sequencers [1, 28]. Conversely, a disadvantage of biological nanopores is their stability, because, due to the fact that they are proteins, they can be denatured by high pH and can be sensitive to salt concentrations [1, 3]. Additionally, the pore sizes available amongst biological nanopores is finite and limited [1].

1.2.2 Solid State Nanopores

Solid state nanopores are advantageous over biological nanopores in that their pore size and channel length can be user defined according to the molecule of interest. Furthermore, they are highly stable and are able to be easily integrated into devices such as microfluidic chips. Solid state nanopores are usually fabricated in a dielectric, inorganic membrane, such as silicon dioxide, silicon nitride, graphene or hafnium dioxide [1, 4]. There are many methods to fabricate solid state nanopores, with the most common being ion/electron beam drilling, dielectric break down and chemical etching.

Focused ion beam and focused electron beam drilling can be used to drill nanopores of varying shape and pore size into different membranes [29]. For example, a focused Ar^+ beam has been used to irradiate a SiN membrane, until enough material was removed that a nanopore formed [30]. Focused electron beam drilling uses an electron beam, for example from a Transmission Electron Microscope (TEM) to erode the membrane, forming a nanopore between 2-200 nm [29, 31]. TEM is more accessible than focused ion beam, and additionally it has a finer resolution so is largely preferred [32]. An advantage to both approaches is that the pore can be monitored during fabrication, and the beam size, duration and position can all be controlled, allowing careful manipulation of the size of nanopore, which can be fabricated to be under 10 nm [2]. Despite these advantages, only one nanopore can be made at a time, and the machinery involved is expensive making them less cost-effective [29, 32].

Another common method is dielectric break down, which involves submerging the membrane into electrolyte and applying a potential difference to the membrane, the strength of the electric field being similar to the dielectric strength of the membrane. This induces leakage current through the membrane and causes dielectric breakdown where the electric field has been applied, causing the formation of a nanopore [2], the size of the pore being controlled by the magnitude of ionic current [32]. Unlike ion/electron beams, this technique is lower cost and more widely available, due to the fact that expensive equipment such as TEM are not required. However, this technique has the same disadvantage as ion/electron beam drilling, in that it is not able to be upscaled [29].

Chemical etching is a method for fabricating solid state nanopores that is both cost-effective and able to be performed on a large scale [31]. An example of a wet chemical etching process involves using photolithography followed by reactive ion etching in silicon nitride films either side of a silicon wafer, to expose windows of silicon. After this, a potassium hydroxide (KOH) solution is used to remove the exposed silicon to form a nanopore [33, 34]. Despite wet chemical etching being cheap and able to be performed on a large scale, the size of each nanopore produced is not identical, because the silicon wafer varies in thickness, the photolithography step is not unwaveringly precise, and there can be bubbles in the KOH solution [29].

Another form of chemical etching is ion track edging, which involves firing heavy ions onto a polymeric substrate to etch tracks into the material. After this wet chemical etching is performed, and the material containing tracks will be etched more quickly than unaffected regions of the material when immersed in the chemical solution [2, 29, 34]. Metal assisted chemical etching involves using silicon as the substrate. The premise behind this technique is that Si coated with metal is etched in chemical solution quicker than bare Si, and the metal particles will descend into the Si and form a nanopore [29].

Solid-state nanopores are advantageous as their pore size and geometry can be modified, and they are more stable, for example to changes in pH, temperature and salt concentrations [1]. However, the pore size and geometry are not as reproducible as for biological nanopores, as slight differences can occur between batches. Furthermore, biological nanopores can be produced on a large scale from cell culture relatively inexpensively, whereas solid-state nanopore fabrication is long and involves more labour and thus is more expensive, however costs are decreasing [1, 3].

1.2.3 Nanopipettes

Nanopipettes are a type of solid-state nanopore that can be quickly and easily produced in a cost effective manner using a benchtop laser puller. Unlike traditional nanopores, nanopipettes can be readily integrated with, for example a piezoelectric positioner, in order to manipulate their x, y and z position. This enables the placement of the nanopore within the nanopipette tip at defined locations, for example for delivery of single entities, and for the integration with scanning ion conductance microscopy, a scanning probe technique [35, 36]. This technique uses the restriction of the ionic current on approaching a cell surface as a feedback mechanism for the position of the pipette, and can be used to generate high-resolution images of live cells in physiological conditions [35, 36]. The topographical map of a cell produced by SICM is generated in real time, and can then be used to position the nanopipette at specific locations on the cell surface, following which the tip can be entered through the cell membrane. The nanopipette can then be used to inject molecules into the cell, by electrophoresis or electroosmosis, driven by the application of a low voltage to the pipette electrode, with long-term survival rates of 92% having been reported [37-40]. On the other hand, a limitation of nanopipettes is that it is difficult to reproducibly fabricate nanopipettes with a pore diameter of less than approximately 15 nm, however nanopipettes with pores below 10 nm in diameter have been reported [41, 42].

Nanopipettes are made from either quartz of borosilicate capillaries, however quartz is predominantly used within the field as it has a higher melting temperature and so can produce nanopipettes with a smaller pore size [16]. The fabrication of a nanopipette using a laser puller is demonstrated in Figure 1.3. A glass capillary is heated at the centre with a CO_2 laser to melt it, following which it is pulled in opposite directions to establish a taper in the pipette. Then, the laser puller heats the centre of the taper, and a hard pull is initiated to pull the capillary into two identical pipettes with a nanoscale-sized pore at the end of the tip [16, 43, 44].

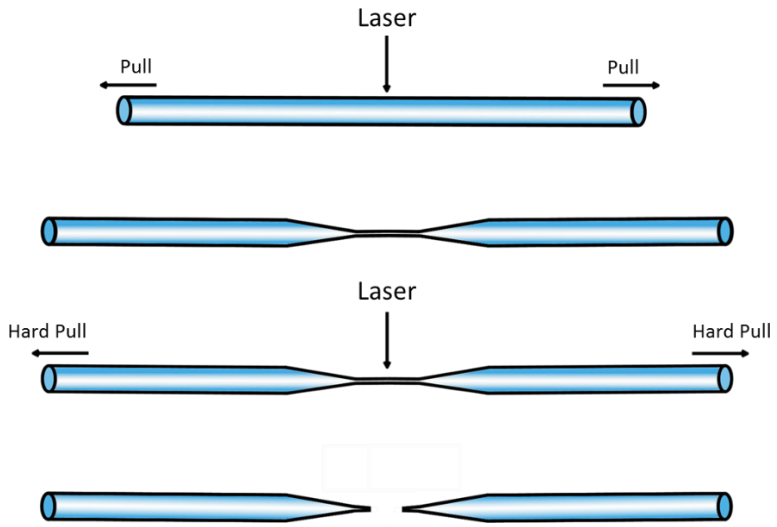

Figure 1.3 Illustration of the laser pulling of a nanopipette starting from a glass capillary. In the first step, a CO_2 laser heats the centre of the capillary, which in turn is pulled to produce a taper. In the second step, the taper region is further heated and a hard pull is initiated, forming two identical nanopipettes.

The pore diameter can be controlled by altering the pulling parameters. These parameters include heat, which controls the power of the laser, and thus the temperature at which the glass capillary is softened. Filament determines the scanning pattern of the laser beam, corresponding to different scan lengths and rate of scan [45]. Velocity controls how fast the puller bar moves before the hard pull. Delay governs the time period between the point at which the laser is turned off and the beginning of the hard pull. Pull controls the force at which the hard pull is executed [16, 45]. Usually a higher heat, pull velocity and force, and a smaller value for delay and filament will lead to a smaller tip [16, 43, 45]. This means that the nanopore size can be tuned to correspond to the size of the molecule being detected, forming a confined space enabling one molecule to pass through the pore at a time, making nanopipettes ideal for label-free single molecule analysis [6, 43].

1.3 Characterisation of Nanopipettes

1.3.1 Geometrical Characterisation

After fabrication, the angle of the pipette at the tip, and its radius can be determined by scanning electron microscopy (SEM) or Transmission Electron Microscopy (TEM) [46], with SEM being the most common way to determine pore size. Figure 1.4(a) shows an example SEM image of a nanopipette. The main parameters of a nanopipette, shown in Figure 1.4(b) are the inner pore diameter (*d*) ,outer pore diameter (*D*) and inner pore angle (θ)

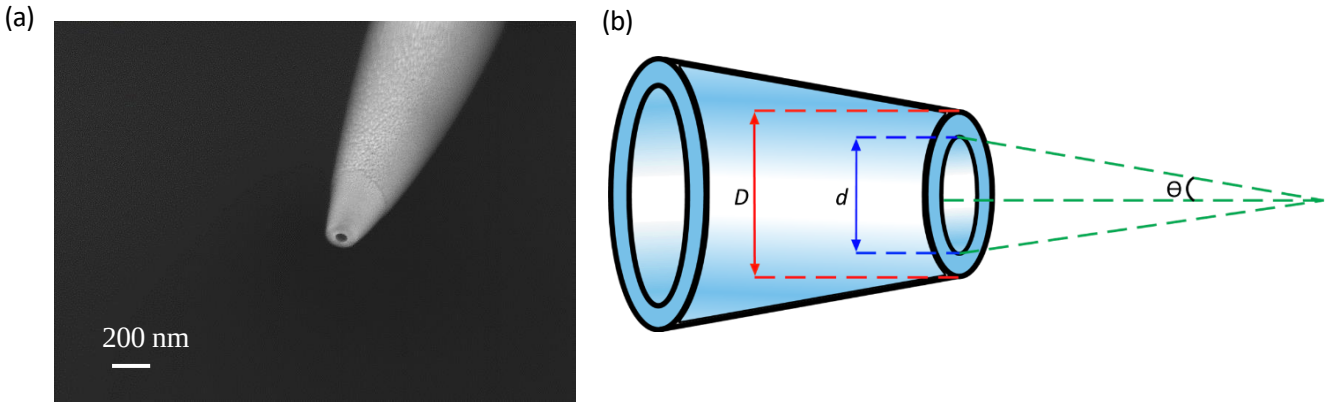

Figure 1.4 (a) SEM image of a nanopipette. Image taken by Samuel Confederat, School of Electronic and Electrical Engineering, University of Leeds and used with permission. (b) Schematic depicting the major parameters of nanopipette geometry: inner pore diameter (*d*), outer pore diameter (*D*) and inner pore angle (θ).

The resolution of SEM is not enough to characterise nanopipettes with a pore diameter below 50 nm. Additionally, a nanopipette of this size must be sputtered with conducting material to minimise charging, which affects the dimensions of the pore [47].

1.3.2 Current-Voltage Measurements

Nanopipettes can also be characterised electrochemically. Because laser pulling produces two identical pipettes, one can be used for geometrical characterisation using, for example SEM, and one can be used to be characterised electrochemically, using IV measurements. The inner

pipette angle (θ) and the resistance can be used to determine the inner radius of the pipette (r_i) using the equation 1.1, adapted from [48] and [49]

$$R_p \cong \frac{\cot(\theta/2)}{\pi \xi r_i} \quad (1.1)$$

Where R_p is the pipette resistance, θ is the inner pore angle, ξ is the conductivity of the solution, and r_i is the inner radius of the pore.

The inner pipette angle (θ) can be estimated from the outer pipette angle (Θ) measured using SEM, using equation 1.2, adapted from [47].

$$\tan(\theta) = \frac{\tan(\Theta)}{r_{o/i}} \quad (1.2)$$

Where θ represents the inner pore angle, Θ the outer pore angle, and $r_{o/i}$ represents the ratio of outer pore radius to inner pore radius.

Calculations using equation 1.1, using simple resistance measurements taken electrochemically to estimate the pipette inner radius show a good correlation to the radii measurements taken with electron microscopy [48].

1.4 Nanopipette Properties

1.4.1 Electrical Double Layer (EDL)

The surface charge of a quartz nanopipette attracts counter-ions in the electrolyte solution, forming a diffuse Electrical Double Layer (EDL) to neutralise the pipette surface charge. The surface charge of the quartz nanopipette depends on pH. As the isoelectric point (pI) of SiO_2 structures are normally within the range of pH 1-4, in an electrolyte solution of KCl (pH 6.8), the pH will be above the pI of quartz, meaning its surface will have a negative charge [50]. The

ions within the electrolyte solution will organise themselves at the surface of the pipette to balance out the charge to form a double layer, the structure of which is illustrated in Figure 1.5.

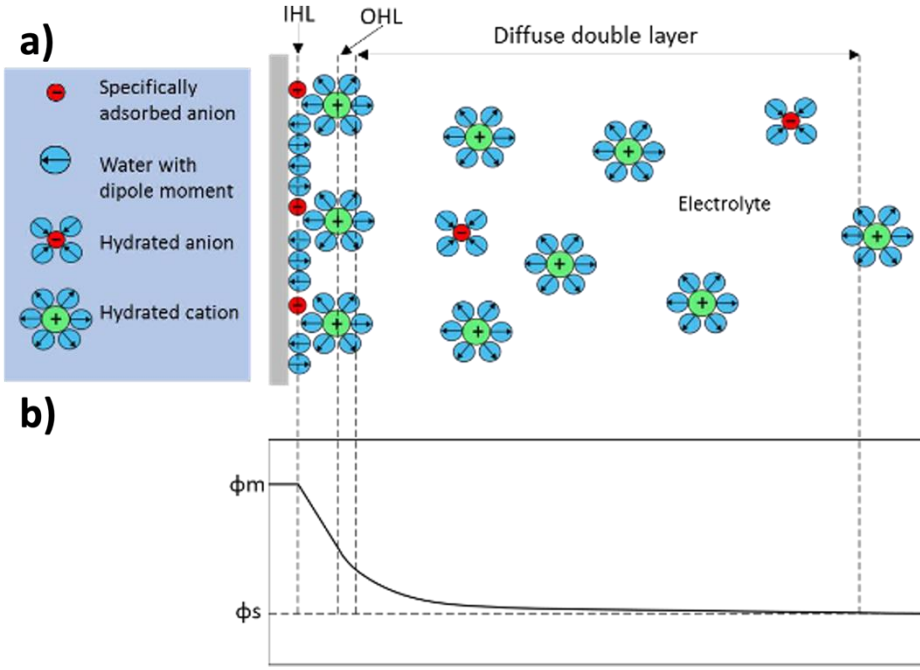

Figure 1.5. a) Illustration of the Gouy-Chapman-Stern Model of the Electrical Double Layer. b) Schematic of the potential across the double layer, where ϕm represents the potential of the surface and ϕs represents the potential of the solution outside the double layer (bottom).

Water molecules are polar, and so they hydrate ions in the solution by surrounding them, and align along the charged surface [51]. In the Gouy-Chapman-Stern model of the EDL, shown in Figure 1.5 there are two layers: an inner layer and an outer layer, the former of which is immobile and the latter diffuse. The inner layer is referred to as the Inner Helmholtz Plane (IHP) and contains ions which are adsorbed to the surface, and so have lost their hydration layer of water molecules. Anions are found more often in the IHP than cations, as they have weaker solvation than cations, and can even adsorb to a surface with a negative charge. The outer layer, the Outer Helmholtz Plane (OHP) is the plane of the closest approach for hydrated ions. Following this is the diffuse double layer, which contains both positive and negative ions and its thickness is determined by the Debye length. The electrical potential

decreases exponentially moving outwards from the surface, illustrated in the graph in the lower portion of Figure 1.5, with ϕm representing the potential of the surface, and ϕs representing the potential of the solution outside the double layer, the potential difference of which ($\phi m - \phi s$) cannot be directly measured [33, 51].

If the EDL thickness is similar to the diameter of the pipette tip, the ionic current must flow through the EDL and the interaction between the charged particles and surface charges influences the passage of the ion flow through the pipette. However, if the EDL is thin compared to the nanopipette tip diameter, the ionic current can flow through the centre of the tip with the bulk electrolyte solution [50]. Both the density of the surface charge of the pipette and the concentration of the electrolyte affect the thickness of the EDL. If the electrolyte concentration is high and the surface charge density is low, the EDL is thinner, and vice-versa. The EDL is usually between 1-30 nm [52].

1.4.2 Electroosmotic and Electrophoretic Transport Through a Nanopipette

In a typical nanopipette experiment, a nanopipette is filled with KCl and immersed in a KCl bath with Ag/AgCl electrodes both within the nanopipette and inside the electrolyte bath. Under the application of a potential difference across the two electrodes, ions are transported across the nanopipette pore, providing the baseline current trace (Figure 1.6, right panel). At the positive anode, Ag is oxidised (equation 1.3), reacting with Cl^- to produce AgCl and an electron (e^-), which flows to the cathode. At the negative cathode, AgCl is reduced by the electron produced at the anode (equation 1.4), which produces Ag and chloride ions (Figure 1.6, left panel) [50].

$$\text{Anode: } Ag(s) + Cl^-(aq) \rightleftharpoons AgCl(s) + e^- \quad (1.3)$$

$$\text{Cathode: } AgCl(s) + e^- \rightleftharpoons Ag(s) + Cl^-(aq) \quad (1.4)$$

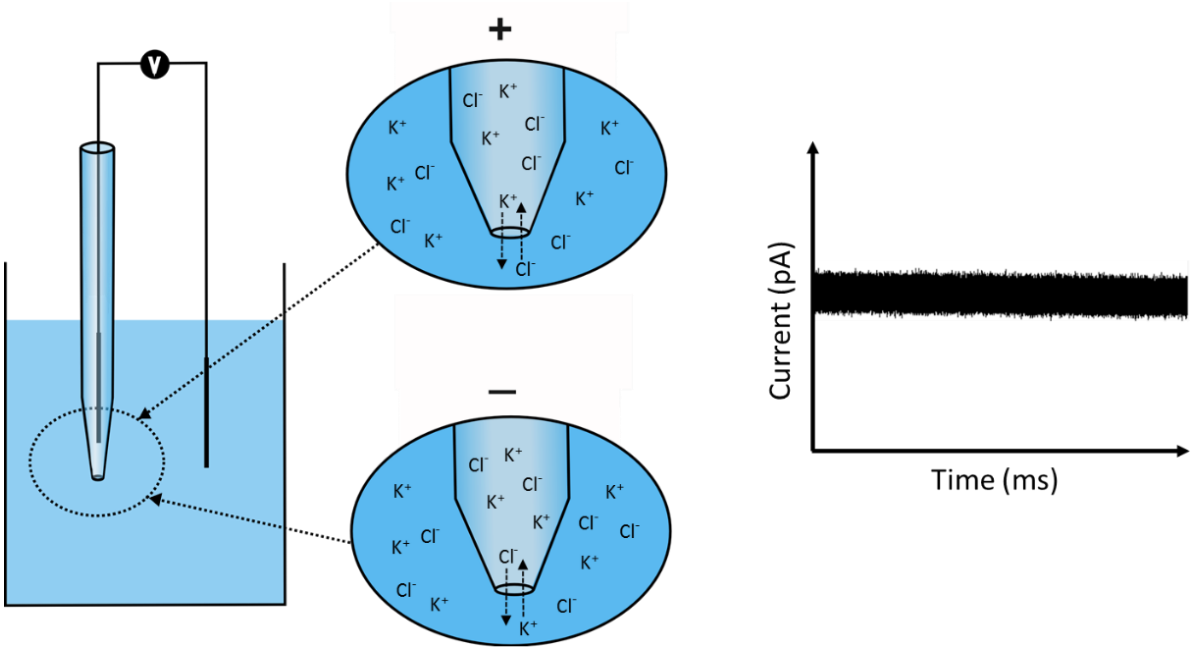

Figure 1.6 Illustration of the movement of ions across the nanopipette pore depending on the polarity of the voltage applied (left) and ion current baseline trace produced by the movement of these ions (right). Under a positive potential at the pipette electrode, silver is oxidised and as chloride ions are taken out of solution, this compensated by a flow of chloride ions into the pipette to replenish them. This is counterbalanced by a movement of potassium ions out of the nanopipette. Under a negative potential applied to the chlorinated Ag pipette electrode, chloride ions are produced by the reduction of Ag in silver chloride, and migrate to the bath electrode, and this is countered by an influx of K^+ into the nanopipette tip.

When potential is applied along a nanopipette which has a surface charge, ions in the EDL next to the pipette surface move. The cations in the EDL draw neighbouring liquid layers along in the same direction towards the cathode, because of viscous interactions. This is referred to as electroosmotic flow [50, 53-55]. On the other hand, electrophoresis is the movement of charged particles in an electric field towards an electrode of opposed charge [55], thus within a nanopipette experiment if, for example, a negatively charged species is inserted into the nanopipette and a negative potential is applied to the pipette electrode, the analyte will move out of the pipette and into the bath.

1.4.3 Ion Current Rectification

The negative surface charge of nanopipettes can lead to current rectification, a phenomenon where the current observed under application of a negative voltage is greater than that observed under a positive bias. Ion current rectification is governed by the concentration of KCl electrolyte. Ohmic behaviour is witnessed for KCl concentrations of 0.1M and above, whereas ion current rectification is observed at concentrations below this. This is because ion current rectification is dependent on the size of the EDL, and the EDL is smaller at higher concentrations of electrolyte. The negative surface charge of a quartz nanopipette means that when a negative potential is applied to the pipette electrode, both the voltage and the surface charge would contribute to movement of Cl^- ions out of the pipette pore, and an influx of K^+ ions into the pipette. Conversely, at a positive bias, cations would move out of the pipette, and if the EDL is large, cations will have to pass through this EDL to leave the nanopipette pore, and their attraction to the negative surface charge will hinder their movement. However, at higher concentrations of electrolyte when the EDL is negligible, ions will move through the neutral zone in the electrolyte at the centre of the tip. The pore size of the nanopipette can also influence the current-voltage characteristics and can lead to ion current rectification. If the EDL is the same size or larger than the size of the nanopore, this can lead to rectification, as the EDL will affect the movement of ions across the nanopipette pore [50]. As the surface charge of the quartz nanopipette depends on the pH of the electrolyte, as too does the ion current rectification, and at the isoelectric point of quartz, the electrical characteristic of nanopipettes follows Ohm's law [16, 50, 56].

Chapter 2- Introduction to Ribosomes and Polysome Profiling

There is much interest in using nanopipettes to detect and analyse biological entities. One such entity is the ribosome. Ribosomes are nanoscale, biological machines composed of RNA and protein, which orchestrate the process of translation, the mechanism by which protein is synthesised in cells. Proteins are essential to life, as they carry out essential functions within a cell. All ribosomes consist of a large and a small subunit; in eukaryotic ribosomes this is the 60S and the 40S subunit respectively, which come together to form the 80S ribosome when translation is initiated [57-60]. An illustration of the structure of prokaryotic and eukaryotic ribosomes is shown in Figure 2.1. This thesis will focus on eukaryotic ribosomes, as they are the centre of the analysis presented in chapter 4.

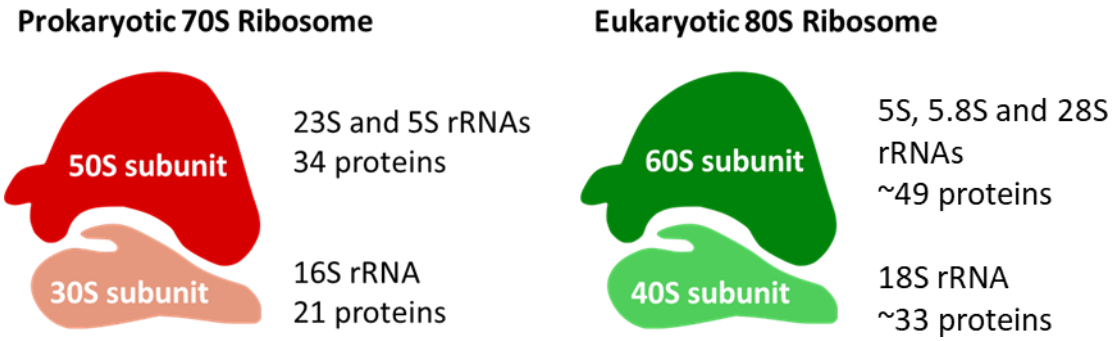

Figure 2.1 A schematic of the structure of 70S prokaryotic (top) and 80S eukaryotic ribosomes (bottom), illustrating the small and large subunits, and the protein and ribosomal RNA (rRNA) contents of each [58].

2.1 Ribosomes and Their Role in Protein Synthesis

For the genetic sequence within DNA to be converted into protein, it must first be converted into an RNA template, called a messenger RNA (mRNA) in a process called transcription. Following transcription, the genetic code on the mRNA molecule is converted into the sequence of amino acids on a protein. This process is illustrated in Figure 2.2.

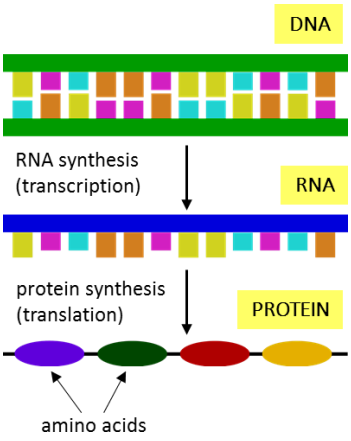

Figure 2.2 Genetic information is converted into proteins by the processes of transcription followed by translation. Transcription involves the synthesis of RNA using the genetic sequence present on the DNA. Translation involves the RNA molecules acting as a template to direct the synthesis of proteins.

Each amino acid is coded for by 3 nucleotides on the mRNA, known as a codon. This is the genetic code, which was decrypted in the 1960s and is universal throughout life on Earth [58]. As there are more possible codons than their amino acids counterparts, the genetic code is redundant, meaning some amino acids have more than one possible codon which code for them [58-60].

To direct an amino acid to the codon encoding it, an adaptor molecule exists which can bind both a specific codon on the mRNA and the amino acid it corresponds to. These molecules are called transfer RNAs (tRNA), the structure of which is shown in figure 2.3. tRNAs are clover-leaf shaped molecules of RNA which fold into an L-shaped 3D structure, with some double-stranded areas and some nucleotides left unpaired. Two important regions are the

anticodon, a three nucleotide sequence which binds to the codon on the mRNA, and a single stranded region where the correct amino acid binds. First, an aminoacyl-tRNA synthetase enzyme recognises a specific tRNA and its corresponding amino acid and covalently links the two. Then, the amino acid is directed to its corresponding nucleotide sequence on the mRNA via base pairing between the codon and the anticodon [58-60].

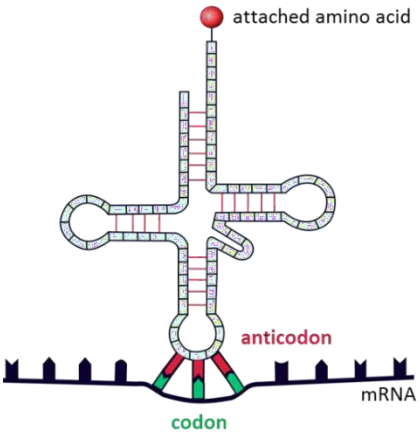

Figure 2.3 An illustration of a tRNA molecule, with the anticodon shown in red base pairing to the codon (green) on the mRNA, and base pairing shown on the double stranded regions (red lines)

The key reaction during protein synthesis is the catalysis of the formation of a peptide bond between the carboxyl end of the emerging polypeptide chain and the amino group on the next amino acid to be added, demonstrated in figure 2.4. The growing polypeptide is always attached to a tRNA molecule, present as a peptidyl-tRNA, and is reformed after each addition of a new amino acid.

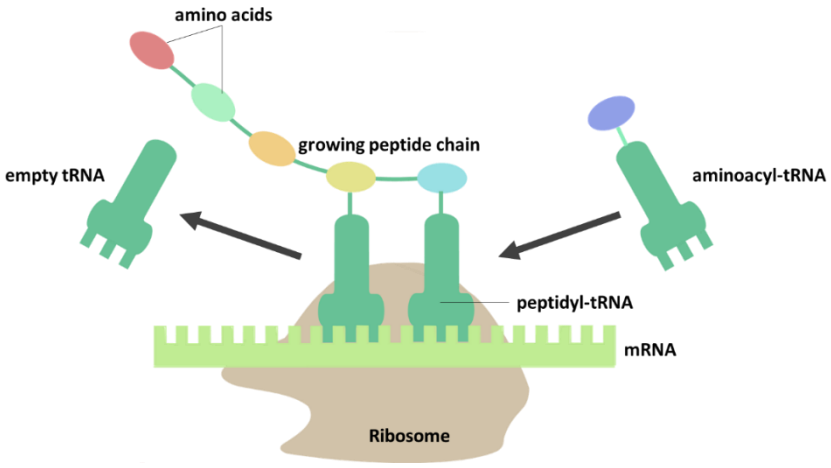

Figure 2.4 The addition of a new amino acid to the growing peptide chain. An aminoacyl-tRNA binds to its codon in the ribosome, for its amino acid to be added to the peptide chain. This causes the previous tRNA to be moved to the exit site and leave the ribosome.

Using a very simplified view of translation that only describes the process of elongation, we can consider four steps to protein synthesis: binding of the RNA (step 1), formation of the peptide bond (step 2), translocation of the large ribosomal subunit (step 3) and finally the translocation of small ribosomal subunit (step 4). The translocation steps cause the ribosome to move along the mRNA to the next codon, where the same cycle can occur again. The process of protein synthesis is outlined in figure 2.5. The ribosome has three key sites, the A-site where tRNAs carrying amino acids (aminoacyl-tRNA) bind, the P-site where the growing peptide chain is present, attached to a tRNA, and the E site, the exit site, where empty tRNAs leave the ribosome. Step one involves an aminoacyl-tRNA base-pairing to the codon present in the A site of the ribosome. This causes it to be in direct alignment to the peptidyl-tRNA present in the P site, for step 2, peptide bond formation to occur. Here, the bond between the polypeptide chain and the tRNA in the P site is broken, and it is attached to the amino acid present in the A site via a peptide bond. This reaction is catalysed by a peptidyl transferase, which is found in the large ribosomal subunit. Step 3 involves the large subunit moving along the mRNA which is still bound to the small subunit, which causes the new peptidyl-tRNA to move to the P-site and the now empty tRNA to move to the E site of the large subunit. In the final step, step 4, the small ribosomal subunit moves to the next codon to join the large subunit. This causes the E site tRNA to be ejected, and the ribosome can now carry out another cycle of the four steps to add a new amino acid to the growing polypeptide chain.

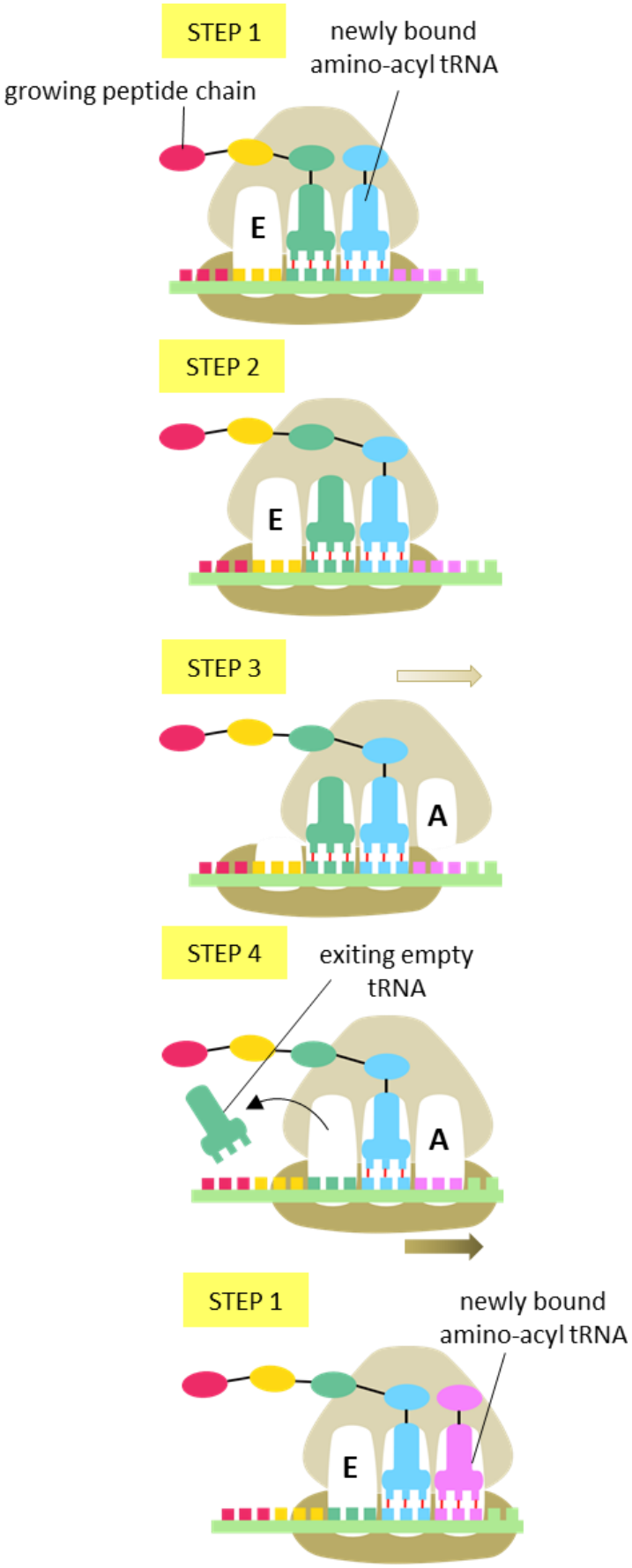

Figure 2.5 A schematic of translation that only describes the elongation phase of translation. In step 1, a new amino-acyl tRNA (blue) enters and binds to the codon in the A site. In step 2, a peptide bond forms between the amino acid on the new tRNA and the growing peptide chain, leaving the tRNA in the P site (green) empty. In step 3, the 60S subunit translocates forward to the next codon on the mRNA, moving the new peptidyl-tRNA (blue) to the P site and the empty tRNA (green) to the E site. In step 4, the empty tRNA exits the E site and the 40S subunit translocates to the next codon. This resets the ribosome for another amino-acyl tRNA to enter the A site for another cycle of the four steps. This is shown in another step 1 (bottom) where a new aminoacyl-tRNA (pink) binds at the A site.

The peptide bond formation is catalyzed by rRNA elements. Additionally, the complex 3D structures of the rRNAs form the core of the ribosome and their 3D structures define the overall shape of a ribosome. Furthermore, it is rRNA which largely creates the tRNA binding sites on the ribosome, and is responsible for the catalytic activity required to form a peptide bond. In this way, ribosomes are ribozymes, a term denoting an RNA molecule with catalytic activity.

Whereas the rRNAs play a key functional role, the ribosomal proteins have a scaffolding function, initially facilitating the assembly of the rRNA core, following which they stabilise it and allow the conformational changes of the rRNA that are needed for catalysis [58-60].

2.2 Polysomes

Single 80S ribosomes can initiate translation on their own, or bind an mRNA molecule without carrying out protein synthesis [60]. However, mRNA molecules which are actively being translated are usually present as polyribosomes (polysomes). This is where several ribosomes bind to an mRNA and carry out protein synthesis at the same time [61, 62]. Usually proteins synthesis can take between 20 seconds and several minutes for the average protein. However, if multiple ribosomes bind to the mRNA one after the other during this time, they can carry out higher rates of protein synthesis than an 80S monosome [58].

Polysomes can be present in various structures, such as double rows, helices and circles. As this thesis centres on the analysis of eukaryotic ribosomes, its focus will remain on polysomes found within eukaryotic cells. Some examples of structures of eukaryotic polysomes are shown in Figure 2.6. In eukaryotes, circular polysomes are formed by interaction between the 5’- and the 3’- end of the mRNA, meaning that upon dissociation of

the ribosomal subunits from the mRNA, they can reassemble again at the start of the same mRNA molecule to complete another round of translation [58, 63]. Circular polysomes are usually the first stage of polysome formation in the cytoplasm, and are considered to be the juvenile form of polysomes [64].

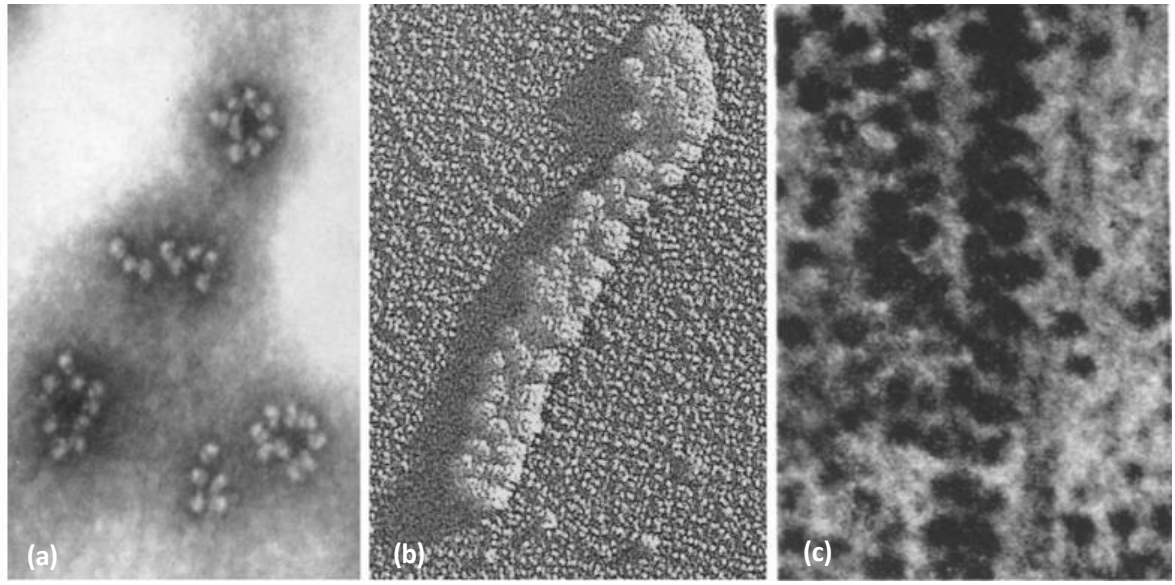

Figure 2.6 Electron micrographs of different structures of eukaryotic polysomes, adapted from [63]. (a) Polyribosomes extracted from mouse tumour cells and negatively stained, (b) Polyribosomes formed in a wheat germ cell-free translation system, platinum shadowed, (c) Section of a cultured eukaryotic cell.

Double-row polysomes are another structure often found, and can be found in linear conformations or collapsed circles. Linear double-row polysomes are actually planar zig-zag structures which, when viewed using electron microscopy (EM) look like a double row, and these forms of polyribosomes can also present with circular polysomes at the beginning of polysome formation as the developing polysome grows [63, 64]. As more ribosomes add themselves to the mRNA to undergo translation, growing circular polysomes can collapse into double-row polysomes that retain the circular conformation, which are also seen as two

parallel rows on EM. Later stages of the life cycle of the polysome involve the de-circularisation of the circular polysomes, forming the linear polysomes that are usually found in the planar zig-zag double row conformation [64].

Bulges can be found in both circular and linear polysomes due to some regions of the mRNA being overloaded by ribosomes, causing dense packing of the ribosomes within that section. Another form of polysomes seen by EM are long tightly packed 3D helices. These bulges can cause the de-circularization of circular polysomes into linear polysomes, and linear polysomes can become the site of nucleation for the formation of the third structure of polysomes commonly seen by EM, densely packed 3D helices [63, 64]

2.3 Polysome Profiling and Translatomics

Transcriptomics (the measurement the global population of RNAs) aims at providing quantitative information about transcripts present in cells at a particular time point and it often focuses on the study of mRNAs. However, not all mRNAs are used to make protein, and the amount of RNA produced does not always mean similar levels of protein will be expressed. It is therefore important to analyse the translatome, which refers to the population of mRNAs that are translated into protein [65]. This can be done by analysing and isolating polysomes, to determine how many ribosomes are bound to an mRNA of interest, or global populations of mRNAs. This can reveal whether, and if so, how efficiently, different mRNAs are being translated, according to the number of ribosomes associated with them, where heavy polysomes (>3 ribosomes) represent efficiently translated mRNAs. In this way,

we can generate a ‘translatome’; the population of mRNAs associated with polysomes, thus being actively translated [65-67].

Profiling polysomes in this manner is done by using sucrose density gradient ultracentrifugation to isolate free RNA, 40S subunits, 60S subunits, 80S ribosomes, and polysomes associated with different numbers of ribosomes into distinct fractions, and is illustrated in Figure 2.7(a) [65-67]. Another alternative is to pool the fractions containing 3 or more ribosomes per mRNA for downstream analysis, as these contain the actively and efficiently translated mRNAs [66, 68].

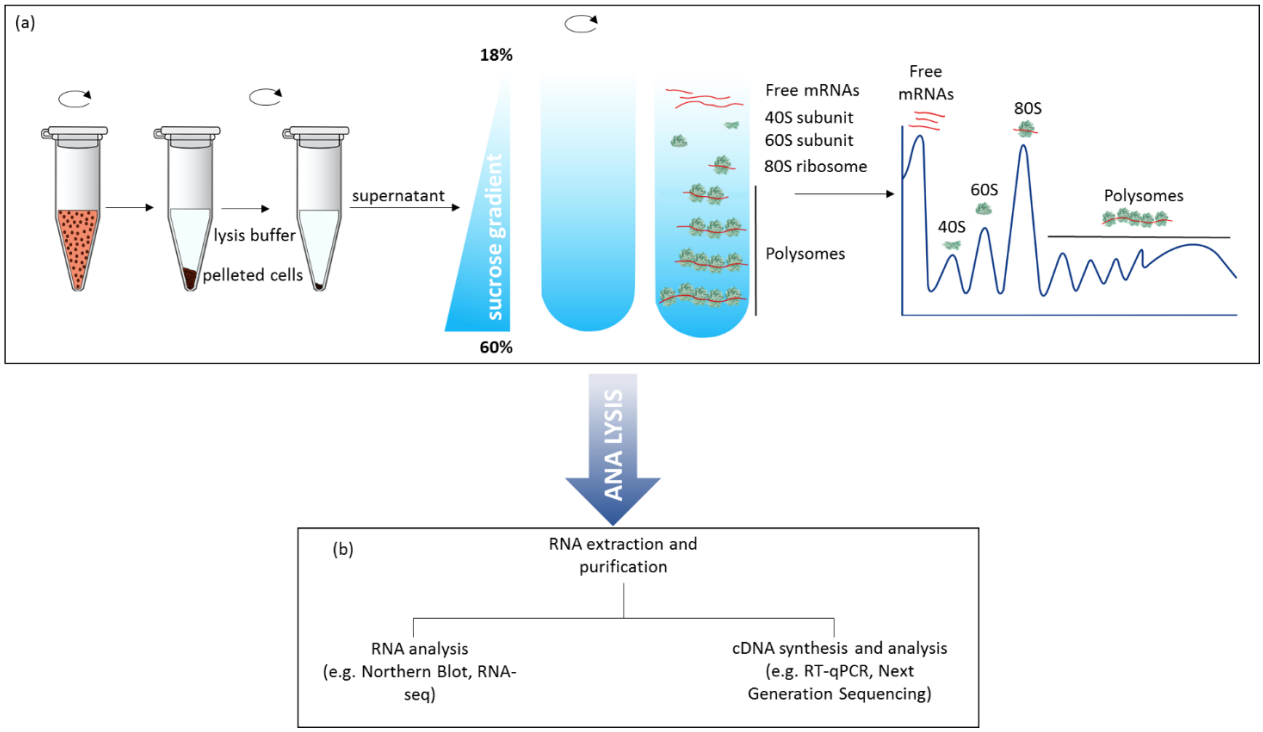

Figure 2.7 A schematic of the polysome profiling process. (a) cells are lysed and pelleted, following which the supernatant is loaded onto a sucrose density gradient and ultracentrifuged. The gradient is then fractionated while monitoring the absorbance at A_{254} using an ultraviolet (UV) spectrophotometer. This separates the gradient into RNAs and low molecular weight complexes, 40S subunits, 60S subunits, 80S ribosomes and Polysomes. (b) Following fractionation, the samples are further extracted and purified for downstream analysis.

The first experiment using sucrose density fractionation to assess polysomes was carried out in the early 1960s [62]. Sucrose density gradient fractionation involves lysing cells, and separating the cytoplasmic lysate on a sucrose gradient, the concentration range of which depends on which type of cell is being lysed. When the preparation is centrifuged, the mRNAs will fractionate with respect to the number of ribosomes that are bound to them (Figure 2.7(a)). Following sucrose density gradient fractionation, the RNA can be isolated from each fraction for downstream analysis (Figure 2.7(b)). This usually involves using Northern Blotting, quantitative reverse transcription polymerase chain reaction (qRT-PCR), microarray or RNA sequencing to quantify the mRNA present in each fraction [66, 68, 69]

For example, polysome profiling has been used to analyse the translational status of *Saccharomyces cerevisiae*, where sucrose density ultracentrifugation was followed by quantitative microarray analysis of 14 fractions. This generated a global profile of the status of translation, by measuring the association of ribosomes with mRNAs from thousands of genes. The authors found that whilst most mRNAs were associated with at least one ribosome, the mRNAs from 43 genes weren't associated with any ribosomes, and that longer mRNAs had more ribosomes associated with them, however, the found that the density of ribosomes decreased with length of mRNA [70].

Aspden et al. used polysome profiling in combination with RNA sequencing, a protocol they termed 'Poly-Ribo-Seq' on *Drosophila melanogaster* cells to assess the translation of small Open Reading Frames (smORFs), which would be translated into peptides fewer than 100 amino acids in length. As smORF mRNA can be occupied by up to six ribosomes, the authors isolated polysome fractions with between two and six ribosomes bound per mRNA. The

actively translated mRNAs were assessed using RNA sequencing, and the RNA sequence was compared to the *D. melanogaster* genome for identification. Aspden et al. identified two types of smORF that were translated, one type coded for a peptides around 80 amino acids in length, the other comprised dwarf smORFs that coded for around 20 amino acids. The method of Poly-Ribo-Seq employed in this study doubled the numbers of smORFS in *Drosophila* S2 cells that were known to be translated, raising the number from 107 to 228 [71].

Although it is considered the gold standard for polysome profiling, sucrose density ultracentrifugation has its limitations. In order to obtain a sufficient yield of separated ribosome fractions, a large amount of starting material is needed. For small tissue samples, such as *Drosophila* organs, obtaining sufficient material for sucrose density gradient fractionation involves weeks of dissection and preparation. Furthermore, the fractionation protocol itself is very time consuming to carry out, due to the long ultracentrifugation step, the duration of which takes hours and can lead to loss of bound proteins [72, 73]. Whilst translatome analysis provides valuable information on the translational status of mRNAs, revealing which genes are actively expressed into protein, there is significantly less literature on translatomics when compared with, for example, transcriptomics. This could be because the protocol for polysome profiling is considerably more labour intensive, and thus can be challenging to upscale for large, high-throughput studies [68]. In addition to this, non-ribosomal complexes have been found in polysome fractions, such as clathrin complexes, as they behave similarly in the centrifugation process [73]. Therefore, polysome fractions obtained from sucrose density gradient ultracentrifugation may not necessarily be homogeneous [72, 73]. Moreover, the fractionation process is done in bulk, which could

potentially mask the true picture of what is happening on an individual ribosome or polysome level due to averaging.

Nanopipettes could offer numerous advantages an alternative approach for detecting separate polysome fractions. Primarily, nanopore experiments are quick, offering an experiment time of minutes, rather than hours. They are also carried out in physiological buffers, with no need for sucrose gradients, and there is no centrifugation step. These factors reduce the likelihood that the structure and integrity of the polysome fractions could be altered, and decreases the chance of bound protein being lost. In addition to this, the ribosomes and polysomes which have been used in a nanopore experiment are ready for downstream analysis immediately. Furthermore, vastly less quantities of starting material are required than in an ultracentrifuge experiment. This is because experiments are performed at the nanoscale level, so only a small volume (<10μl) and concentration of sample is required, meaning sample preparation time is greatly reduced and experiments are appropriate and straightforward for rare or small tissue samples. In addition to this, nanopipettes are cheaply and easily produced, and both fabrication and experiments can be carried out on a bench top. In contrast to this, the ultracentrifuge is a very expensive, specialist piece of machinery that may not be available in all laboratories. Importantly, nanopore experiments are performed on the single molecule level, and thus collect data for each individual ribosome or polysome, and aren't confounded by averaging. This moreover would facilitate accurate counting of individual polysomes and ribosomes to assess the translational status of a cell.

Chapter 3- Review of the Literature

3.1 Analysis of RNA and Ribonucleo-complexes Using Nanopores

Wanunu et al employed solid-state nanopores, with a diameter of 3-3.5 nm have been used to investigate the interaction between a model of the prokaryotic ribosomal A-site RNA with aminoglycoside antibiotics, which target this site and interrupt protein synthesis by blocking tRNA binding, and/or limiting the reliability of codon-anticodon recognition [74]. Using the ionic current signal trace, it was observed that the peak amplitude increased with increasing concentrations of paromomycin, and it was possible to distinguish between complexes of the A-site RNA and the drug, and the A-site alone. This is demonstrated in Figure 3.1 which shows histograms of the mean peak amplitudes taken for increasing concentrations of paromomycin. Before addition of paramycin, two populations are visible in the distribution of peak amplitude, corresponding to translocations of the A-site RNA, and collisions with the nanopore (blue). As the concentration of paromomycin increases, the amount of A-site RNA present in complex with the drug increases also, and a third population appears with a higher peak amplitude, corresponding to the drug:RNA complex (red). When the paromomycin concentration increases to 130 μm, the number of events in the third population increases (purple). The authors found that despite the increase in peak amplitude upon adding paromomycin, there was no significant increase in dwell time [74].

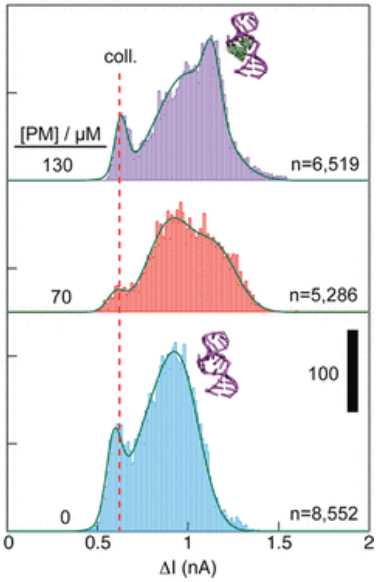

Figure 3.1 Histograms of the peak amplitude for events corresponding to 0 μM paromomycin (blue), 70 μM paromomycin (red), and 130 μM paromomycin (purple). As the concentration increases, the number of RNA/drug complex increases, as does the population of events corresponding to the complex in the histogram, and the mean peak amplitude increases also. Adapted from [74]

Astier and co-workers [75] investigated the reversible binding of RNA to an adenosine triphosphate (ATP)-dependent bacteriophage packing motor protein, P4, using an α-hemolysin pore. First, nanopore translocation experiments were carried out using a synthetic oligoribonucleotide (5'-$C_{25}A_{25}$-3'), and current blockades were observed. The authors were able to distinguish RNA molecules which entered the vestibule of the α-hemolysin pore, but did not continue to traverse through the inner narrow stem, which were represented by a 50% block of the current, whereas complete translocation of an RNA molecule through the pore was denoted by an almost complete blockage of the baseline current for the duration of the translocation. Next, the effect of P4 binding on the translocation speed was investigated. A solution containing 0.5 μM P4 and 0.5 μM of the $C_{25}A_{25}$ oligoribonucleotide was added to the *cis* chamber of the nanopore, leading to events with high peak amplitudes with both short dwell times and long dwell times. The short events were determined to be the translocation of $C_{25}A_{25}$ only, as the peak characteristics were comparable to the previous experiments, and the longer events were hypothesised to be due to P4:RNA complexes, with the oligoribonucleotide part of the complex being threaded through the pore, a schematic of this complex is shown in Figure 3.2. When ATP was added, the long events almost disappeared, returning to a baseline level comparable to that witnessed with RNA only, suggesting the motor activity of P4, which requires ATP to function, results in a move from the P4:RNA complex to free RNA [75].

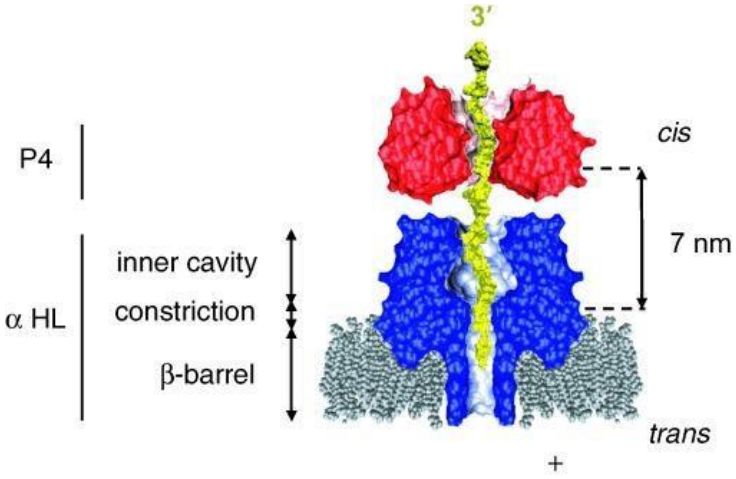

Figure 3.2 The theorised interaction between P4 (red) and α-hemolysin (blue). The schematic shows α-hemolysin within a lipid bilayer. The golden thread is the oligoribonucleotide 5'-$C_{25}A_{25}$-3', which threads through P4 and the pore of α-hemolysin. Adapted from [75].

To test the theory that the oligoribonucleotide part of the P4:RNA was spanning the α-hemolysin pore in the longer events, the authors used P4 in complex with different length RNAs. Short oligoribonucleotides (C_{10} and C_{15}) did not result in long, high amplitude events, which is to be expected as they are not long enough to cross both the P4 binding site and the

narrow stem of the α-hemolysin pore. For the oligoribonucleotide C_{30}, long events were observed, as expected, due to it being long enough to span both the P4 binding site and the full pore. However, they were not witnessed in as high frequencies as for $C_{25}A_{25}$, because the P4 motor protein can bind to any site on the RNA, which would lead to some C_{30}:P4 complexes which did not have free RNA that was long enough to span both the P4 protein and the pore. Following this, it was investigated whether or not the ratio of $C_{25}A_{25}$:P4 affected the translocation events. The presence of events is caused by the RNA entering the protein pore, and so if $C_{25}A_{25}$ was bound by two P4 proteins, then the remaining RNA strand would not be long enough to enter into the α-hemolysin pore, and so would decrease the frequency of events. 0.5 μM of $C_{25}A_{25}$ was added to the cis chamber, with either a 1:0, 1:1 or 1:4 ratio of $C_{25}A_{25}$:P4, and indeed, a decrease in events was observed as the concentration of P4 was increased [75].

Nanopores have been used to detect the conformational change which occurs when a benzimidazole drug binds to a region of Hepatitis C viral RNA. Upon binding the drug, the RNA changes from a bent structure to a linear, straight structure. When the RNA is translocated across a nanopore in the absence of the drug, or with a control benzimidazole which does not illicit a conformational change, there is a wide range in dwell times, the longer ones also exhibiting high peak amplitudes, therefore blocking more current. This is because the bent structure makes it difficult for the RNA to translocate the pore, and the longer events represent RNA molecules which have become lodged in the pore, and therefore block more ion flow, leading to an increase in the current blockade. However, when a mixture of the drug and the RNA is translocated across the pore, all resulting current signatures have very short dwell times, due to the conformational change making it easier for the RNA to cross [76].

In 2015, the same group demonstrated the application of a nanopore to be able to detect different tRNA molecules using their ion current signature. In this work, two different tRNA molecules were passed through a biological nanopore, and the investigators were able to discriminate between them. However in this experiment, the tRNA molecules were unravelled prior to translocation, and thus were not analysed in their *in vivo* conformation [77]. Building on this work, Henley *et al.* analysed tRNA molecules in their native 3D fold

by using a nanopore which allowed the tRNA molecule to pass through, but was small enough to induce the tRNA molecules to deform upon translocation. The authors showed that each of 5 tRNA molecules produced a characteristic peak and noise spectrum, and machine learning was used to identify each tRNA molecule from the different characteristics of their respective current blockade, with 88% accuracy. This study shows the potential for nanopores to be employed to study tRNA flexibility and dynamics in the future, as the tRNA has to change conformation to pass through the nanopore, and thus its stability may affect the peak characteristics [78].

Nanopores have also been utilised to investigate RNA folding. For example, the mRNA of gene 32 from a T2 bacteriophage (T2 RNA) forms a pseudoknot structure. To study the folding of the pseudoknot, the T2 RNA was passed through a nanopore, during which it unfolded into a single strand, meaning its folding could be studied in comparison to its fully unfolded state. Poly$(CAT)_{10}$ DNA tags were added to both ends of the T2 RNA, and the 3' end of the resulting molecule was biotinylated, to which streptavidin was attached. This meant that when the resulting hybrid molecule passed through the nanopore from *cis* to *trans*, the streptavidin blocked the molecule from travelling any further and arrested it within the nanopore. However, as the 3' DNA is longer than the nanopore itself, the T2 RNA is allowed to move through the nanopore and into the *trans* electrolyte solution, where it can fold without being constricted by the nanopore. The process of the experiments is elucidated in Figure 3.3. The authors held the unfolded RNA in the *trans* electrolyte solution for fixed intervals, and then applied a negative voltage to pull the RNA back through the nanopore to the *cis* side. This meant the folding could be arrested at any intermediate structure or at the pseudoknot itself. The characteristics of the resulting current blockade, in combination with coarse-grain molecular dynamics simulations and the master equation approach was used to deduce the structure of the intermediates and the folding pathway of the RNA was resolved [79].

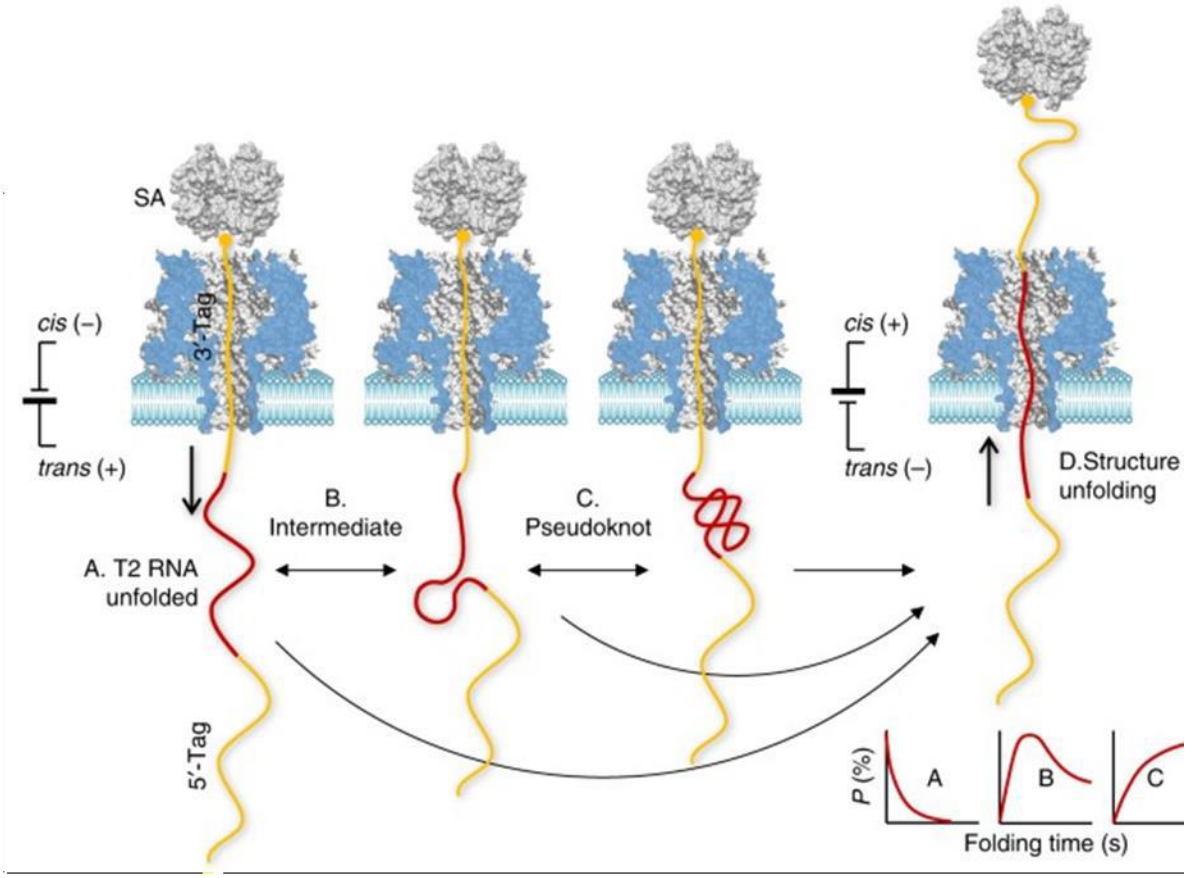

Figure 3.3 Nanopore characterisation of the folding of T2 RNA using a biological nanopore. The T2 RNA has a 5'-DNA tag, and a 3'-DNA tag. The 3'-tag is attached to streptavidin (SA), which immobilises the complex. When immobilised, the T2 RNA folds in the *trans* electrolyte solution. After a pre-determined time, the folding is arrested in an intermediate state (B) or at the folded pseudoknot structure (B). This is done by using a negative voltage, which disrupts the folding by threading the T2 RNA back through the pore. The current signatures reveal the folding (B and C) states, as well as the unfolded state (A). The pseudoknot folding pathway is determined by the appearance of the folding states over a set time. Adapted from [79].

3.2 Ribosomes in Nanopore Research

50S bacterial ribosomal subunits have been detected by the ion current blockades generated by their translocation across a solid state nanopore within a microfluidic chip. The set up of the microfluidic chip is illustrated in Figure 3.4(a). The nanopore had a diameter of 45 nm, and was fabricated through etching followed by ion beam milling on a SiO_2/Si_3N_4 layered

film. During each experiment, a solution containing 50S ribosomal subunits was introduced to the central reservoir, and when a voltage was applied across the microfluidic channel and the nanopore, the ribosomal subunits would translocate across the pore, and a current blockade would be detected. A cross section of the microfluidic channel with analyte translocation is shown in Figure 3.4(b) [5].

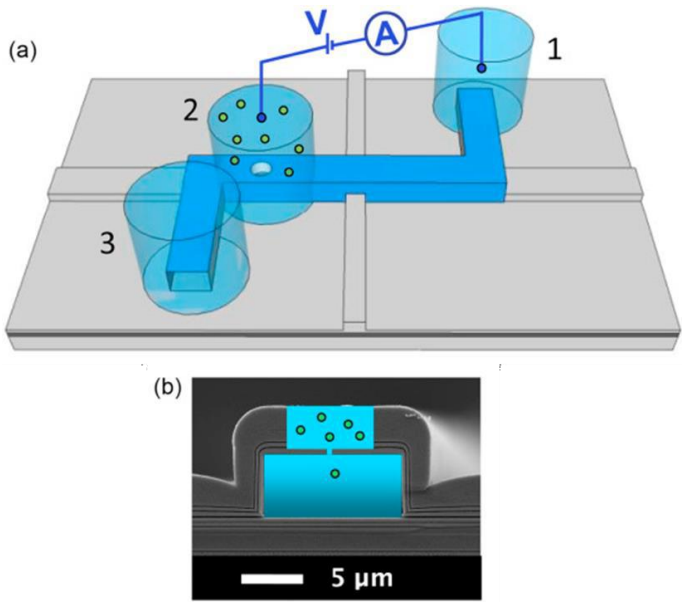

Figure 3.4 (a) A schematic of the Z-shaped microfluidic channel, with three reservoirs, the nanopore being integrated below the middle reservoir (2). (b) Cross section of the microfluidic channel showing the nanopore integrated below the central reservoir. Adapted from [5].

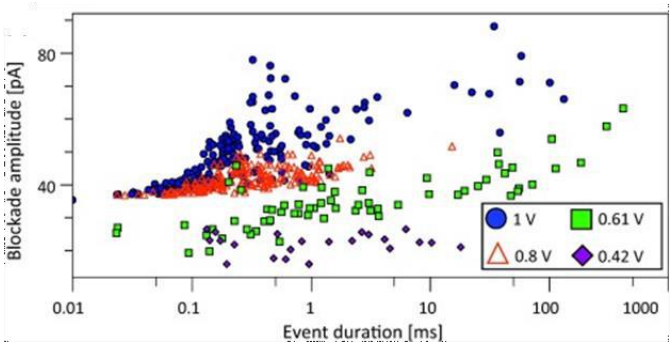

Figure 3.5 Peak amplitude versus dwell time scatter plot for four different voltages- 0.42 V represented by purple diamonds, 0.61 V by green squares, 0.8 V by red triangles and 1 V by blue circles. As seen in this diagram, the peak amplitude increases overall with voltage. Adapted from [5].

The authors analysed the characteristics of the current blockades in terms of peak amplitude and dwell time for four different voltages, 0.42V, 0.61V, 0.8V and 1V (Figure 3.5) and found that the peak amplitude was linear dependent to the voltage. The scatter plots of the blockade amplitude as a function of the event duration show a large distribution of translocation times, which could be due to different translocation characteristics, such as the subunits 'crawling'

through in the longer dwell times. In figure 3.5, it appears that some of the events with longer duration have higher peak amplitudes, which could be explained by two ribosomal subunits translocating the pore at a time, and when translocated under a lower applied voltage, the ribosomes may be adhering to the wall of the nanopore along the way [5].

Following the determination of the peak amplitude and dwell time characteristics of the ribosomal subunits, the authors assessed whether they could control the translocation of the subunits into the microfluidic chip, to make it a single-file manner, in order to use the device for the controllable capture of single subunits for further analysis. First, the frequency of events depending on the voltage was investigated, as shown in Figure 3.6.

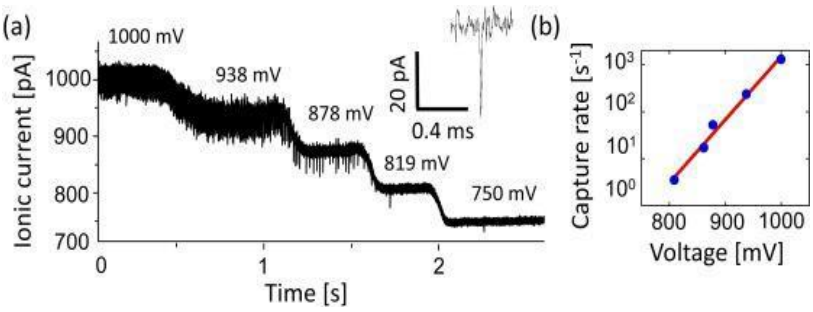

Figure 3.6 (a) Ion current traces under different applied voltages showing the appearance of distinct current blockades at 878 mV .
(b) Plot of the relationship of the number of translcation events per second (Capture rate) as a function of voltage on voltage, which is shown to be an exponential relationship. Taken from [5].

Below a threshold of around 800 mV, the events disappear, and the authors found that they appear again when the voltage is increased above this threshold. This behaviour was exploited to allow the capture of a single ribosomal subunit. To do this, the voltage is progressively increased until a translocation event is observed. When the required number of entities have been captured, the voltage is lowered below the threshold voltage, and the single ribosomal subunits can be trapped in the reservoir below for downstream analysis [5].

Following this, the same group designed an optofluidic chip device containing a solid state nanopore fabricated using focussed ion beam (FIB) milling through alternating layers of SiO_2 and Ta_2O_5. The design of the chip is shown in Figure 3.7. Within the optofluidic chip, the microfluidic channel, which acts as a liquid-core optical waveguide, is connected to solid-

core waveguides, where fluorescence is excited by the solid-core waveguide and is collected

by the liquid-core waveguide. At the ends of the channel there are reservoirs, where sample materials can be introduced. In addition to these reservoirs, reservoir 2 shown in Figure 3.7 is placed above a nanopore, and single particles can be introduced into the liquid-core waveguide through voltage-driven translocation across the nanopore, via application of a voltage between reservoirs 1 and 2 [80].

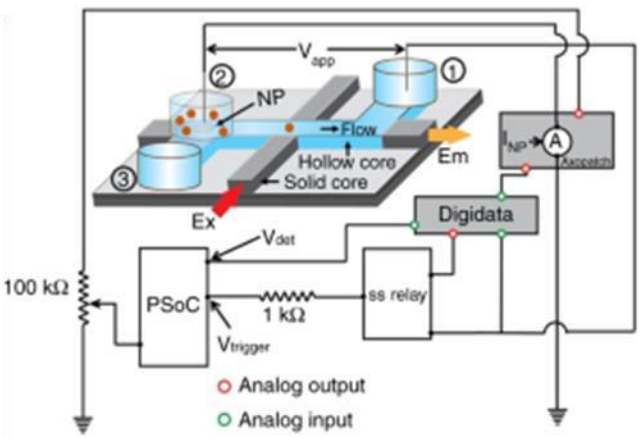

Figure 3.7 A schematic of the optofluidic chip. The liquid-core waveguide is shown in blue, and the solid-core in grey. When a voltage is applied between the first and second reservoirs, single particles enter the liquid-core waveguide. Feedback control over the number of particles to translocate the nanopore is executed by connecting the chip to an electronic circuit. Adapted from [80]

A microcontroller within a solid-state relay, shown in Figure 3.7 was added to the chip to add feedback control over the number of particles crossing the pore. This was achieved by the fact that the microcontroller analyses the current passing through the nanopore in real time. When the current is measured to be above a pre-defined threshold level defined by the authors, a translocation of a single particle is recorded, however the threshold is such that fluctuations in the baseline are ignored. After a pre-selected number of entities have translocated the nanopore, the voltage is switched off, stopping any further molecules traversing. As shown in Figure 3.8(a), the authors demonstrated the controlled delivery of a single 70S bacterial ribosome through a nanopore with a diameter of 38 nm, with the top panel demonstrating the current and the bottom showing the applied voltage. After the current returns to baseline level after a single translocation, the voltage is turned off so no more molecules can enter, trapping a single particle in the analysis area of the chip.

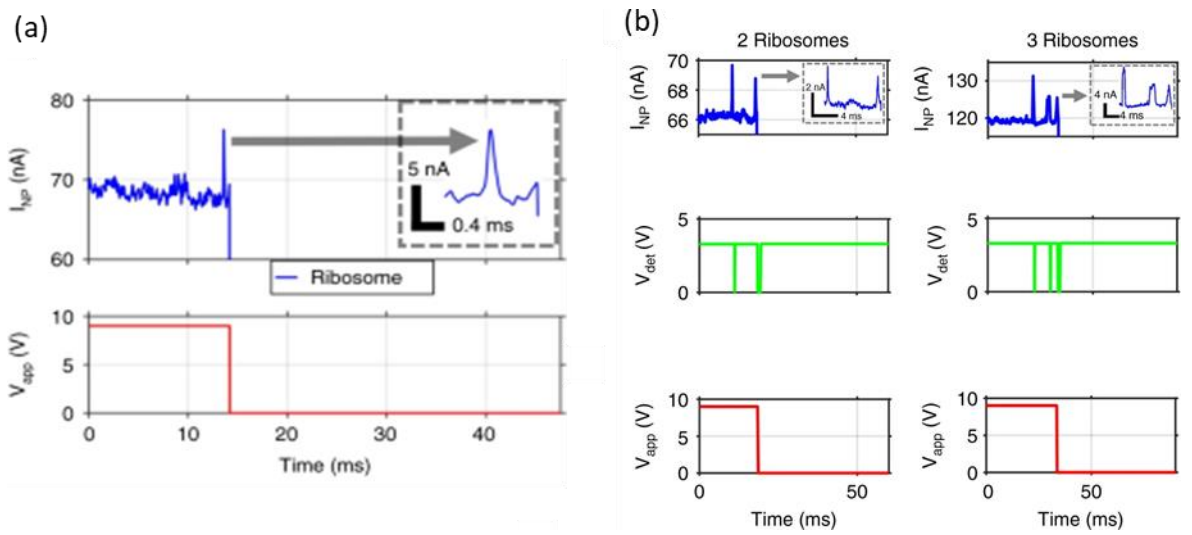

Figure 3.8 Translocation of single ribosomes, modified from [80] (a) Introduction of a single 70S ribosome into the microfluidic channel, the top panel showing the current passing through the nanopore, and the bottom showing the voltage applied. The insert in the top panel shows a zoomed in current blockade, indicative of a single translocation. (b) Translocation of two and three ribosomes into the microfluidic channel, numbers which had been pre-defined. The top panel shows the current traces for translocations, the centre panel demonstrates the signals of identification of single particle translocation within the detection circuit, and the bottom panel demonstrates the voltage applied across the pore which is switched off after the pre-determined number of entities have traversed the pore and been detected.

The feedback control was also programmed to turn the voltage off after a pre-selected quantity of 70S ribosomes had translocated the pore. This is shown in Figure 3.8(b) in which both two and three ribosomes are allowed to traverse the pore into the microfluidic channel before the voltage across the pore is switched off. Additionally, after translocation occurs, the voltage across the pore can remain switched off for a pre-defined amount of time, before it is raised again and the pore is 're-opened'. This could be used to automate the process, once the time frame for the analysis of the molecule traversing the pore is known, the time that the pore is switched off can be aligned with this, to allow controlled capture of single molecules that is automated [80].

Additionally, it was investigated whether the pore could be selectively gated for λ-DNA molecules, when introduced as a mixture with 70S ribosomes. In this sense, the voltage across the pore would only be switched off if DNA traversed it, meaning that for example the

DNA could be used for further analysis whereas other contaminants within the solution would be ignored. To do this, the ion current peak amplitude and dwell time characteristics generated when either 70S ribosomes or λ -DNA molecules translocated the pore were analysed, so that they could be used for the identification of the distinct molecules in the mixture. Scatter plots generated from the experiments involving translocation of 70 ribosomes only and λ-DNA only are shown in Figure 3.9(a). It was determined as a result of these control experiments that current events with a peak amplitude lower than 10 nA, and a dwell time under 0.8 ms were due to λ –DNA molecules. This ion current profile generated for the DNA molecules was then used to selective gate λ –DNA in a mixture of both DNA and ribosome molecules.

In this way, as a translocation event occurred, the dwell time and peak height were monitored, and if the characteristics corresponded to the event characteristics of λ –DNA, the nanopore was voltage gated immediately, so no other molecules could cross. This was conducted with a mixture of 70S ribosomes and λ –DNA. The translocation characteristics observed in such experiments with the DNA ribosome mixture is shown in the scatter plot in Figure 3.9(b), with the peak amplitude and dwell time thresholds (10 nA and 0.8 ms) shown by dotted lines. This was also achievable for selective gating of the 70S ribosomes in the mixture, by using their distinctive ion peak characteristics [80].

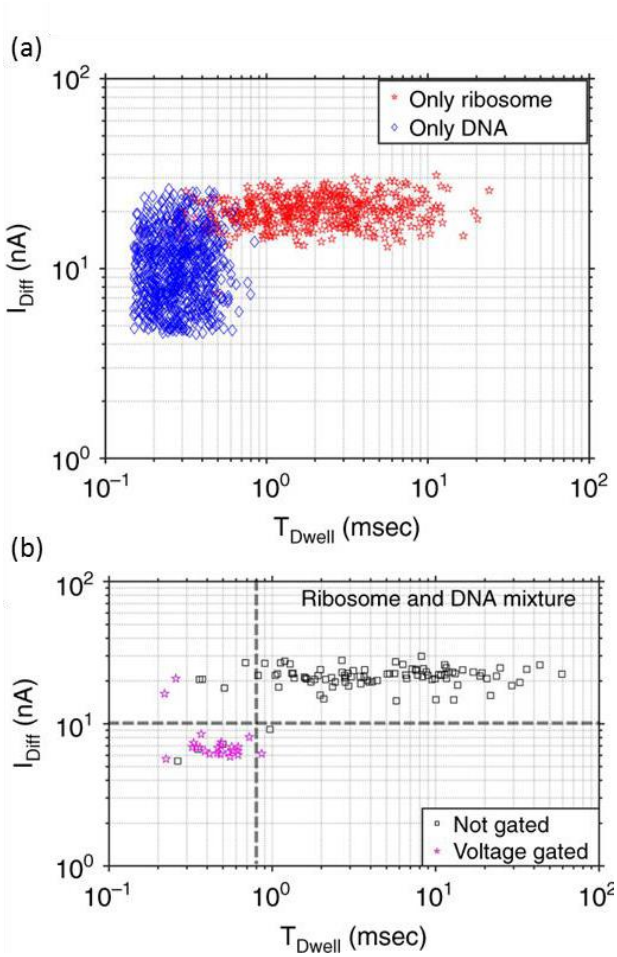

Figure 3.9 Selective gating of λ –DNA from a mixture of λ –DNA molecules and 70S ribosomes. (a) Scatter plot of peak amplitude against dwell time for separate translocation experiments where only 70S ribosomes (red) and only λ –DNA (blue) was used to traverse through the nanopore. (b) Scatter plot of peak amplitude vs dwell time for translocation experiments performed on a mixture of λ –DNA molecules and 70S ribosomes. The magenta stars indicated events which were followed by voltage gating, and those in represented by black circles were not. The thresholds used to determine gating are notated by the dotted lines. Adapted from [80].

In my 2020 paper, in collaboration with Mukhil Raveendran and Paolo Actis, School of Electronic and Electrical Engineering, University of Leeds, and Tayah Hopes and Julie Aspden, Faculty of Biological Sciences, University of Leeds, we published the first comprehensive study demonstrating the detection and analysis of ribosomes and polysomes at the single-entity level using a nanopore [81]. In this paper, we showed that nanopipettes could be used to detect individual 80S ribosomes and polysomes of differing sizes, using the characteristic ion current blockades generated as they traverse the pore. This was validated in *D. melanogaster* embryonic and ovary samples, as well as a human cell line. In addition, a fingerprint for 80S ribosomes was generated, enabling detection of 80S ribosomes in a mixed sample. Large polysomes with more than 7 ribosomes attached to a single mRNA were also able to be differentiated from lighter polysomes, with a significant difference between the peak amplitude of the ion current signature. All experiments were carried out in sample volumes of >5μL, meaning only a small starting quantity of sample was necessary, enabling analysis of scarce samples, such as *D. melanogaster* ovaries. This work provides a solid

foundation for nanopipettes to be used as a bio-analytic tool for polysome profiling in the future, with short experiment times, single-molecule resolution and small sample volumes [81]. The results of this work will be discussed in detail in Chapter 5.

Chapter 4- Materials and Methods

4.1 Nanopipette Fabrication

Nanopipettes were produced by laser pulling quartz glass capillaries with an inner diameter of 0.50 mm and an outer diameter of 1.00 mm and a length of 7.5 cm (QF100-50-7.5, World Precision Instruments, UK) with a Sutter instrument P-2000 laser puller. The laser pulling process is detailed in Chapter 1, however nanopipettes were pulled to achieve a nanopore diameter comparable in size with the molecule of interest. For the ribosome and polysome experiments in Chapter 5, nanopipettes with a diameter of ~60 nm were used, and the laser pulling program used to produce them was a two line protocol, shown in table 4.1, and IV curves generated by such pipettes are shown in Figure 4.1(a). Pipettes used in experiments performed by Mukhil Raveendran, School of Electronic and Electrical Engineering, University of Leeds, in [63] were fabricated using the two line programme shown in table 4.2, also resulting a diameter of ~60 nm. Representative IV curves for such pipettes are shown in Figure 4.1(b). For the RNA virus experiments in Chapter 6, the pulling protocol was a two line programme shown in table 4.3, to produce a pore of approximately ~20 nm in diameter. Example IV curves demonstrated by such pipettes are shown in Figure 4.1(c). The pore sizes were estimated by measuring the resistance of the pore, and for the pipettes used in [63] were characterised by Mukhil Raveendran using Scanning Electron Microscopy (SEM). The working and reference electrode were made from Ag/AgCl wires of 0.25 mm diameter (Sigma-Aldrich, U.K.)

Table 4.1: Pulling parameters for production of nanopipettes with a pore diameter of ~60 nm, and a resistance of around ~130 MΩ using quartz capillaries with an outer diameter of 1.0 mm and an inner diameter of 0.5 mm

HEAT	FIL	VEL	DEL	PULL
775	4	30	170	80
825	3	20	165	180

Table 4.2: Pulling parameters used in experiments by Mukhil Raveendran in [63] for production of nanopipettes with a pore diameter of ~60 nm and a resistance of around ~130 MΩ, using quartz capillaries with an outer diameter of 1.0 mm and an inner diameter of 0.5mm

HEAT	FIL	VEL	DEL	PULL
775	4	30	170	120
900	3	20	175	180

Table 4.3: Pulling parameters for production of nanopipettes with a pore diameter of ~20 nm in diameter, with a resistance of ~190 MΩ, using quartz capillaries with an outer diameter of 1.0 mm and an inner diameter of 0.5 mm

HEAT	FIL	VEL	DEL	PULL
750	4	30	150	80
700	3	40	135	148

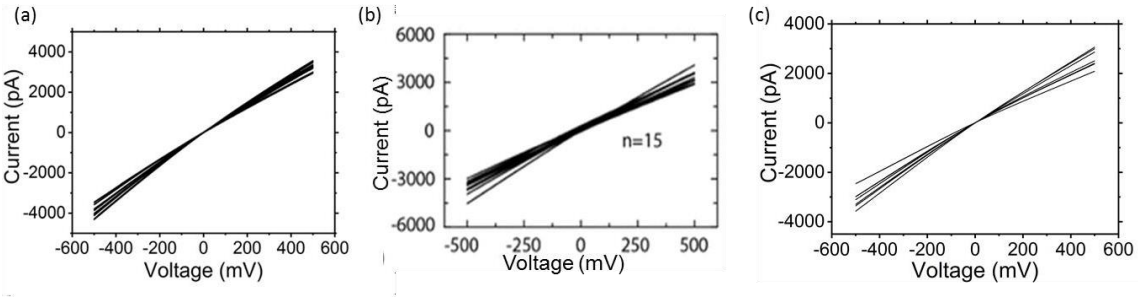

Figure 4.1 IV traces for (a) pipette programme used in Chapter 5, representative of 10 pipettes (b) pipettes used by Mukhil Raveendran, image modified from [81] (c) nanopipettes used in Chapter 6, representative of eight pipettes.

4.2 Ion Current Measurements

For the experiments with ribosomes and polysomes in Chapter 5, nanopipettes were filled with a 0.1 M KCl and 10 mM $MgCl_2$ solution (Sigma Aldrich, USA), containing the ribosome or polysome sample of interest to a final concentration of 20μg/ml. Magnesium was added to stabilise the ribosomes and polysomes. Experiments carried out by Raveendran in our paper
[81] were carried out in 0.1 M KCl only, as the absence of magnesium ions was found to have no effect on polysome stability within these experiments. For the Chikungunya virus (CHIKV) replicon experiments in Chapter 6, nanopipettes were filled with 1x Tris-EDTA (TE) buffer, 0.1 M KCl (Sigma Aldrich, USA) and the CHIKV RNA at a final concentration of either 300 pM, 30 pM, 6 pM or 3 pM.

The nanopipette was fitted with a working electrode, and then submerged in an electrolyte bath, within which the reference electrode was immersed. In each experiment, the electrolyte bath matched the electrolyte solution present in the pipette. During the ribosome/ polysome experiments in Chapter 5, when a positive voltage is applied to the pipette (working) electrode, the ribosomes move from the inside of the nanopipette, through the nanopipette pore, and into the bath solution, causing a modulation in the ion current. These experiments were carried out at an applied voltage of +600mV. For the replicon experiments in Chapter 6, when a negative voltage is applied to the nanopipette electrode, the CHIKV RNA replicons move from inside the nanopipette, across the pipette pore and into the bath solution. The passage of the replicon through the nanopore causes an amplification in the ion current trace, which is seen as events which are recorded for analysis. The delivery of the RNA replicon was performed under an applied voltage of -400mV. Figure 4.2 shows a schematic of the nanopipette set up, where an applied voltage causes the polysomes or the CHIKV RNA replicons to exit the pipette.

The ion current data were obtained using a patch-clamp system from Axon Instruments (Molecular Devices, USA). Measurements were recorded using an Axopatch 700b amplifier, and data were acquired at a sampling rate of 100 kHz and low pass filtered 20 kHz.

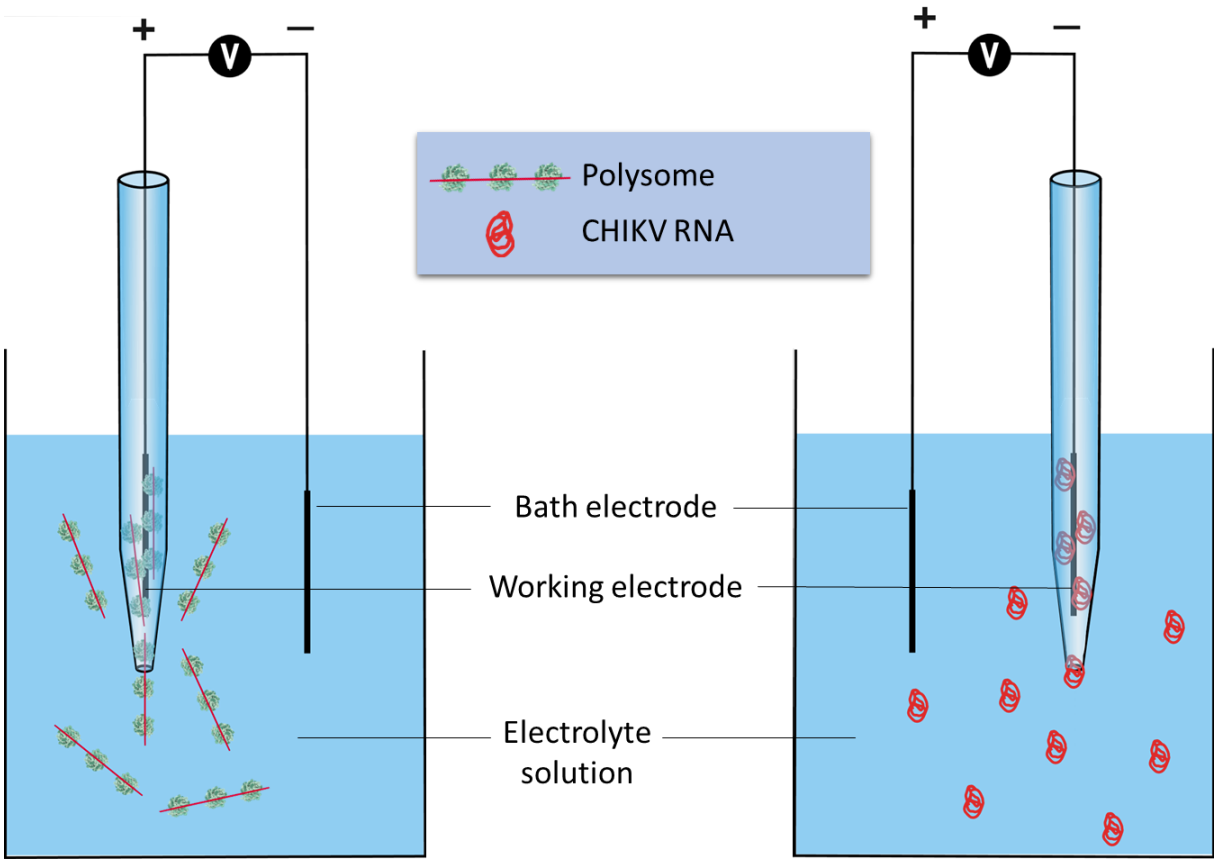

Figure 4.2 Schematic showing the nanopipette set up for Chapter 5 experiments (left) and the Chapter 6 experiments (right). The bath contains a bulk electrolyte solution to which an electrode is fitted, and the nanopipette is filled with an electrolyte solution containing the sample of interest and is fitted with a working electrode. When a voltage is applied, the biological entity traverses the nanopipette pore into the bath solution.

4.3 Data Analysis

4.3.1 Analysis of ion current

Data were analysed using custom MATLAB software (Prof. Joshua Edel, Imperial College London, UK) and further analysed using Origin 2017 (OriginLab, USA) and RStudio (RStudio, USA). The MATLAB code identifies translocation events, selecting the modulations in current with a peak amplitude greater than a threshold of 7 standard deviations above the level of the baseline noise. In order to define the baseline, an asymmetric least square smoothing algorithm is used, and the baseline fit is defined by a

Poisson probability distribution function. The start and end points of a single event are defined by the first and last points of data above the baseline level. The dwell time and peak amplitude of each event is then extracted and converted into an Excel spreadsheet, and these data were used to create the scatter plots, box plots and statistical analysis shown in Chapter 5 and 6. This further data analysis was created using Origin 2017 and RStudio. All accompanying images in this thesis were created using Inkscape 1.2.1 (Inkscape, USA).

4.3.2 Statistical Analysis

Statistical Analysis in Chapter 5 was performed using RStudio (RStudio, USA). The values for peak height were transformed using a boxcox transformation to normalise the data, where $\lambda = -0.9$. A linear model was generated for the transformed peak height values as a factor of polysome fraction. Following this, an analysis of variance for the linear model was generated to determine if there was a significant difference in the values for peak height.

4.4 Ribosome Preparation

Ribosomes were prepared by Tayah Hopes in the Aspden Group, Faculty of Biological Sciences, University of Leeds.

4.4.1 Cell Culture

S2 embryonic and ovary cells were grown in Schneider's Media containing L-glutamine (Sigma-Aldrich, UK) to which 10% fetal bovine serum (Sigma-Aldrich, UK), 25 μg/mL amphotericin B 100 U/mL penicillin and 100 μg/mL streptomycin (GE Healthcare, UK) were added. The cells were kept at 26°C in adherent, non-vented flasks (Sarstedt, Germany)

4.4.2 D. melanogaster Husbandry

Wild type *D. melanogaster* (Dahomey) were reared on sugar-yeast agar and kept in 6 oz square bottom bottles (Flystuff, UK) at 50% humidity and at 25°C with a light/dark cycle of 12:12h.

4.4.3 Purification of Ribosomes

Each step of ribosome isolation and purification was carried out at 4°C or on ice. Ovaries were harvested in 1 x Phosphate-buffered saline (PBS) (Lonza, Switzerland) and 1 mM dithiothreitol (Sigma-Aldrich, UK) and 1 U/µl RNasin Plus (Promega, UK) from females aged 3-6 days, and then were flash frozen in liquid nitrogen. To disrupt the ovaries, 1.5mL of RNAse-free pestles (Scientific Laboratory Supplies, UK) were used in lysis buffer, which contained 50 mM Tris-HCl at pH 8 (Sigma-Aldrich, UK), 150 mM NaCl, 10mM $MgCl_2$ (Fluka, USA), 1% IGEPAL (Sigma-Aldrich, UK), 1 mM dithiothreitol, 100 µg/mL cycloheximide, 2 U/µl Turbo DNase (Thermo Fisher, UK), 0.2 U/µl RNasin Plus and 1 x ethylenediaminetetraacetic acid (EDTA)-free protease inhibitor cocktail (Roche, Switzerland). Before harvesting, 100 µg/mL cycloheximide (Sigma-Aldrich, UK) was used to treat them for 3 minutes. The cells were pelleted for 8 minutes at 800 *g*, after which they were washed in 1 x PBS with 100µg/mL cycloheximide. The cells (both S2 and ovary) were lysed for 30 minutes in 500 µl of the lysis buffer, after which they were centrifuged at 17 000 *g* for 5 minutes, removing the nuclei.

The resulting cytoplasmic supernatants were loaded onto 18-60% sucrose gradients and ultracentrifuged for 3.5 hours in a SW40Ti rotor (Beckman Coulter, USA) at 170 920g and at 4°C. A Gradient Station (Biocomp Instruments, Canada) with fraction collector (Gilson, USA) and Econo UV monitor (Bio-Rad, UK) was used to collect 0.5 mL of fractions. These fractions which were combined according polysome number. Fractions were then diluted to 10% sucrose, concentrated using a 30 kDa column (Amicon Ultra-4 or Ultra-15 (Merck, Germany)) and buffer exchanged (50mM Tris-HCl at pH8, 150mM NaCl, 10mM $MgCl_2$), until a final sucrose concentration of ≥0.1% was reached. Samples were diluted 20-fold in a filter sterilized solution of 0.1 M KCl and 10 mM $MgCl_2$ as single-use aliquots, and then frozen in liquid nitrogen. Following this, aliquots were stored at -80°C, and defrosted on ice and kept at 4°C when required for experiments.

4.5 Viral RNA preparation

CHIKV-nsP4-GAA-FLuc-SGR Chikungunya viral replicon RNA was prepared by Siu Lee, a PhD student under the supervision of Prof. Mark Harris in the Faculty of Biological Sciences, University of Leeds.

4.5.1 Endonuclease digestion

To linearize CHIKV replicon DNA for in vitro transcription, 10μg of the replicon DNA was digested with the appropriate restriction enzyme and incubated at 37°C overnight. The replicon was about 10,000 bases in length. Where needed, the resulting digested DNA was treated with Calf Intestinal Alkaline Phosphatase (CIP) to prevent vector re-ligation. To achieve this, 10 units of CIP was added to the reaction mixture and incubated for 1 hour at 37°C

4.5.2 In vitro transcription

Capped RNA synthesis of CHIKV replicons was performed using mMESSAGE mMACHINE SP6 Transcription Kit (Ambion) using the manufacturer's protocol, using 1μg of linearised CHIKV replicon DNA. The RNA synthesised was quantified using Nanodrop, using absorbance ratio at 260/280 nm, and was subsequently analysed on a 0.1% 3-(N-morpholino)propanesulfonic acid (MOPS) gel. Following this, the RNA CHIKV replicons were stored in single use aliquots in diethyl pyrocarbonate (DEPC)-treated water at -80°C.

Chapter 5- Detection and Characterisation of Ribosomes Using Nanopipettes

All experiments and preliminary analysis were performed by myself, and this data lead to the hypothesis and conclusions of the paper I published in collaboration with Mukhil Raveendran, Tayah Hopes, Julie Aspden and Paolo Actis [81]. Further statistical analysis and validation studies were carried out by Mukhil Raveendran as presented in [81] but the original experiments, conclusions and hypothesis are my own. All unpublished data displayed in this thesis were carried out by myself.

5.1 Single Entity Detection of S2 80S Ribosomes

In order to establish whether nanopipette could be used to detect and analyse 80S ribosomes and polysome fractions, nanopipette translocation experiments were performed. In each experiment, a nanopipette was filled with the ribosome or polysome sample in 0.1 M KCl and 10 mM $MgCl_2$, using a microloader. The working electrode was fitted into the nanopipette, and the reference electrode was fitted to a bath containing the same electrolyte solution as the nanopipette. Following this, the nanopipette was immersed in the bath to complete the circuit. When a positive voltage is applied to the working electrode inside the nanopipette, the ribosomes translocate across the nanopipette pore, which causes a constriction in the ion current as the complexes pass through the pore. This is demonstrated in downwards peaks in an ion current trace, as shown in Figure 5.1(a), called events. Each ion current trace for each experiment was recorded for two minutes. Quartz nanopipettes with pore diameter ~60 nm were used. Nanopipettes were fabricated using a laser puller, with a 2-line pulling parameter programme (see Chapter 4), which resulted in pore sizes which were highly reproducible, demonstrated in the current voltage graphs in Figure 5.1(b).

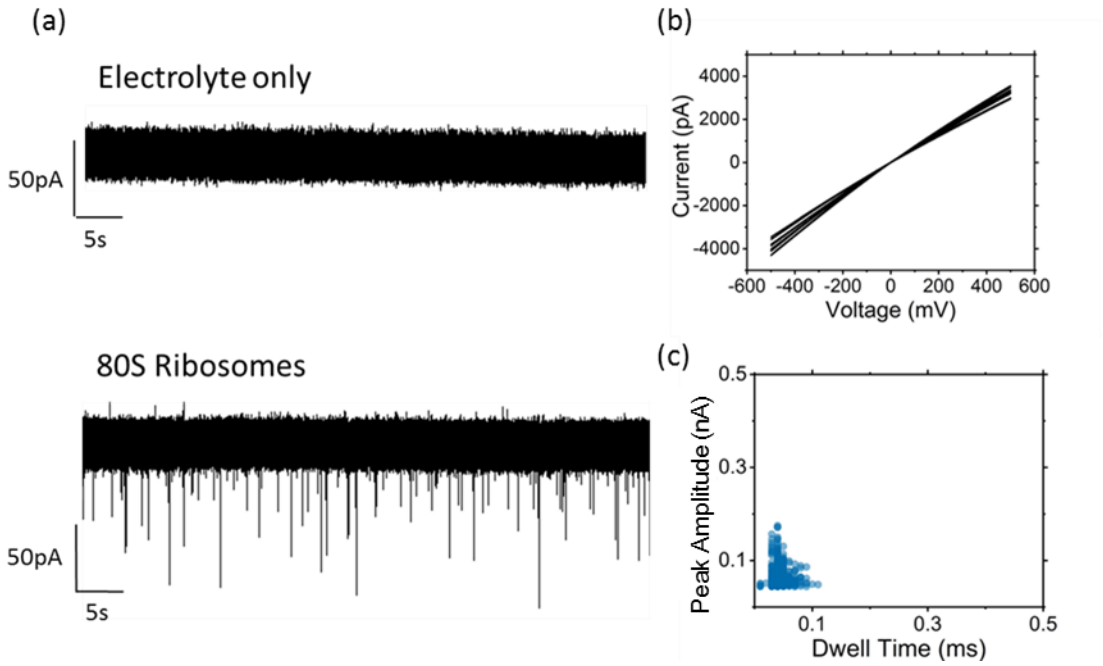

Figure 5.1 (a) Representative Ion current traces with electrolyte alone (top) and in the presence of *D. melanogaster* S2 embryonic cell 80S ribosomes (bottom). When 80S ribosomes are added to the nanopipette, there are modulations in the ion current which resemble downwards peaks. Each peak, or event, is caused by 1 ribosome passing through the pore of the nanopipette tip. (b) I-V graphs taken from 10 different nanopipettes fabricated using the same pulling parameters. (c) Scatter graph of peak amplitude vs dwell time for >100 events taken from an 80S ribosome sample. The ion current trace shows an inhomogeneous peak amplitudes indicating possible contamination of sample with higher molecular weight complexes (i.e. light polysomes).

I first analysed 80S ribosomes from *D. melanogaster* S2 embryonic cell lines to test the hypothesis whether the nanopore platform is able to detect the translocation of single ribosomes. As shown in figure 5.1(a), in the absence of 80S ribosomes, with only electrolyte present in the nanopipette, the ion current trace is steady and unchanging. However, upon the addition of 80S ribosomes to the pipette, under a positive voltage, ribosomes traverse the nanopipette pore and cause a temporary decrease in the ion current as they pass through. This is shown as downwards peaks, or events, in the ion current trace. Each translocation event is indicative of one 80S ribosome traversing the pore, as this is a resistive pulse experiment, more than one ribosome travelling through the pore at the same time would result in a much greater amount of the ion current flow being obstructed, and thus result in a higher peak amplitude, whereas Figure 5.1(c) indicates the peak amplitudes are clustered together, hence demonstrating the effectiveness of nanopipettes to be used for single-entity detection for 80S ribosomes. Under a negative voltage, the ion current trace resembles the trace observed in the absence of ribosomes, as there are no events. As the ribosome has an overall negative charge, due to the rRNA composition, one would expect them to traverse the pore electrophoretically

under a negative bias. However, as events are observed only under a positive voltage, the translocation must be driven by electroosmosis [52]. This observation is intriguing as we do not expect electroosmotic force to be strong enough to drive the translocation of such large complexes but I did not investigate this effect further during my thesis.

Each event was selected above a threshold of 7σ from the baseline noise level, and thus each peak can be said to represent a single 80S ribosome traversing the nanopore with a high degree of confidence, which illustrates the ability of this nanopore platform to detect ribosomes with single-entity resolution. The characteristics of >100 events showed a mean dwell time of 0.04 ± 0.01 ms, and a mean peak amplitude of 0.07 ± 0.01 nA. Figure 5.1(c) shows a scatter plot of the peak amplitude and dwell time of events derived from a 2-minute trace taken from an 80S ribosome sample containing >100 events. The events exhibit a cluster with similar characteristics and thus suggest each event is from a single population. All experiments were repeated on multiple nanopipettes (at least 3) and all findings were also corroborated by experiments performed by Dr Mukhil Raveendran.

5.2 Detection and Analysis of S2 Polysomes

After establishing the ability to detect 80S ribosomes, I investigated the ability of the nanopipette platform to differentiate between different polysome fractions. First, polysomes were isolated from *D. melanogaster* S2 embryonic cells and separated by sucrose density fractionation. Figure 5.2(a) shows the UV profile across the sucrose gradient illustrating the separation of the different fractions, and Table 5.1 illustrates the naming of each fraction.

Table 5.1: Naming of polysome fractions in accordance with the number of ribosomes present on each strand of mRNA in the fraction.

Polysome Fraction	Number of Ribosomes Bound per mRNA
R1	1 (80S ribosome)
R2	2
R3	3
R4	4
R5-6	5-6
R7-11	7-11
R11+	>11

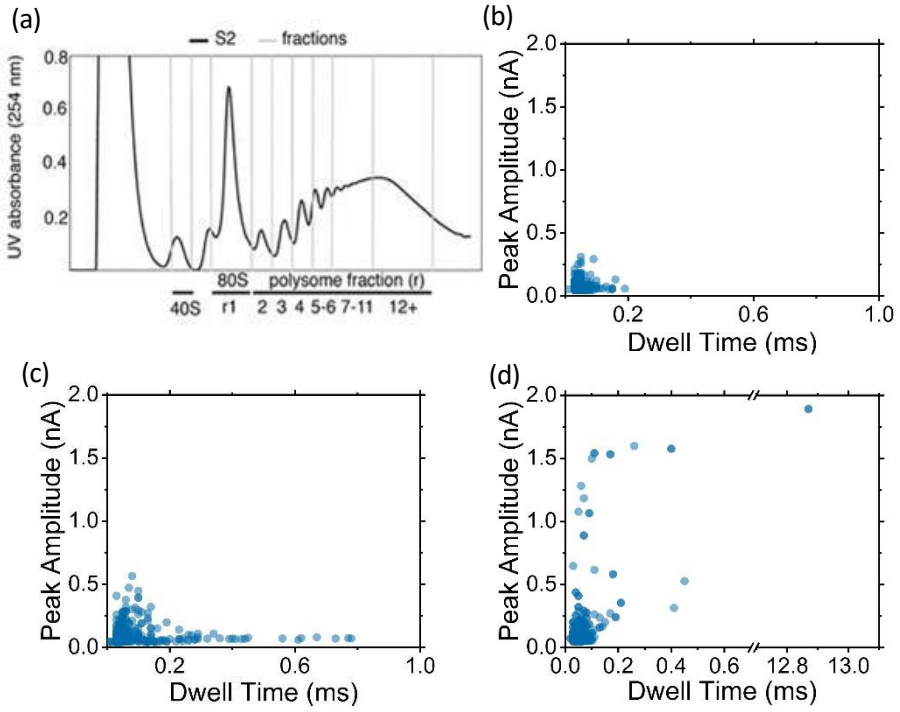

Figure 5.2 (a) UV (254 nm) profile across the sucrose gradient, where ribosomal complexes are separated according to size, which causes them to sediment at different points along the sucrose gradient. Ribonucleic proteins and RNA stay at the top of the gradient and 40S, 60S then 80S ribosomes follow, and then polysomes with different numbers of ribosomes bound to each mRNA strand. (b) Peak amplitude against dwell time scatter plot for R2 polysomes taken from >100 events. (c) Peak amplitude against dwell time scatter graph for R4 polysomes, using >100 events. (d) Scatter plot of peak amplitude against dwell time for R11+ polysomes, taken from >100 events.

The nanopore experiments for polysome samples were carried out with the same experimental set up as described previously. The characteristics of >100 events per sample were analysed and R2 polysomes showed mean dwell time of 0.05 ± 0.01 ms and a mean peak amplitude of 0.08 ± 0.01 nA, R4 polysomes showed a mean dwell time of 0.09 ± 0.01 ms and a mean peak amplitude of 0.11 ± 0.01 nA, and R11+ polysomes showed a mean dwell time of 0.09 ± 0.02 ms and a mean peak amplitude of 0.14 ± 0.01 nA. All experiments were repeated on multiple nanopipettes (at least 3) and all findings were also corroborated by experiments performed by Dr Mukhil Raveendran. These results demonstrate a trend that as ribosome number increases, as does peak height, which is further exemplified in the scatter plots for a 2 minute trace of each polysome sample containing >100 events (Figure 5.2(b-d)). This could be due to the fact that as the ribosome number increases, the polysome samples occupy a larger volume in the nanopipette pore, and so are able to block a greater magnitude of ionic current as they pass through. Furthermore, as ribosome number increases, the range in peak height is more widespread too, as demonstrated in Figure 5.2(b-d) and the boxplots for peak amplitude shown in Figure 5.3, with R11+ showing a very wide range of peak heights. This could be because R11+ is a heterogeneous sample.

Additionally, there appear to be overlapping populations from sample to sample, which could be due to mRNA molecules that have overlapping numbers of ribosomes bound in each fraction. Statistical analysis (see Chapter 4) showed that there was a significant difference in the peak heights of all polysome samples when compared to R1 ribosomes (P <0.001), a significant difference between R2 and R4 polysomes (P = 0.0063) and a significant difference between the R4 and R11+ polysomes (P = 0.012). These results were corroborated by Mukhil Raveendran in our joint paper [81], who found a significant difference (P <0.001) between the peak heights of R2, R4 and R11+ polysomes, and a significant difference with peak heights from R4 (P = 0.03), R5-6, R7-11 and R 11+ (P < 0.001 for each) polysome samples when compared to 80S ribosomes.

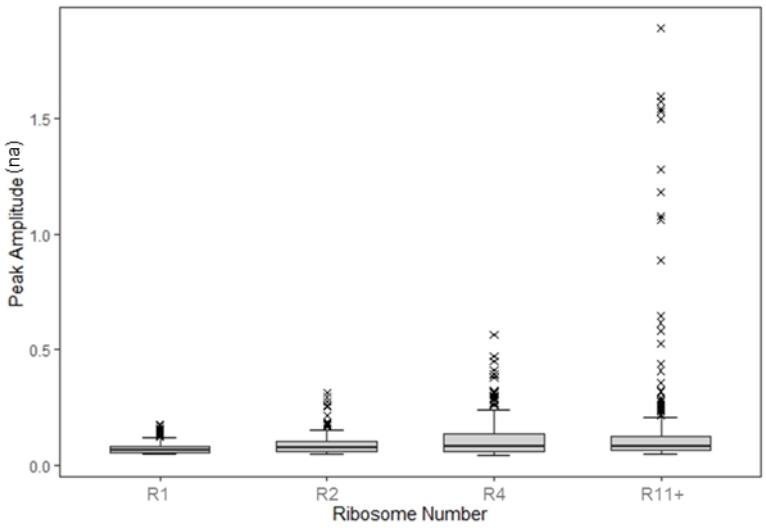

Figure 5.3 Boxplots showing the median value and lower quartile and upper quartile of peak amplitudes for R1, R2, R4 and R11+ samples. Data for each sample taken from >100 individual events.

As seen in Figure 5.2(b-d), and in the box plots in Figure 5.4, the dwell times for each sample are more widespread as ribosome number increases, and there are some events which have increasingly long dwell times, although this isn't as well reflected in the mean dwell times for each sample. In particular R11+ shows one event with a dwell time of 12.87 ms, which is considerably higher than the dwell times of all other events. The longer dwell times displayed by some events could be due to the longer polysomes traversing the pore in either a circularised or linear conformation and possibly getting stuck at the nanopipette tip. Another explanation could be more than one polysome traversing the pore at the same time. An increase in the magnitude and variability of dwell time and peak amplitude for R11+ samples is expected due to the fact that it contains polysomes with differing numbers of ribosomes bound per mRNA, in differing conformations. However, the widest range of dwell times is exhibited by R4. This could be because R4 ribosomes form a certain conformation which will block the pipette pore for longer, or conversely that the R4 ribosomes are in a linear chain which will limit the ionic current for a longer period of time. This large distribution for R4 ribosomes was not seen upon repeat experiments by Mukhil Raveendran [81], and so could be due to particular features of either the sample or the particular nanopipette in this experiment that lead the ribosomes to become lodged within the pore more often. A significant difference in dwell times was not observed between fractions.

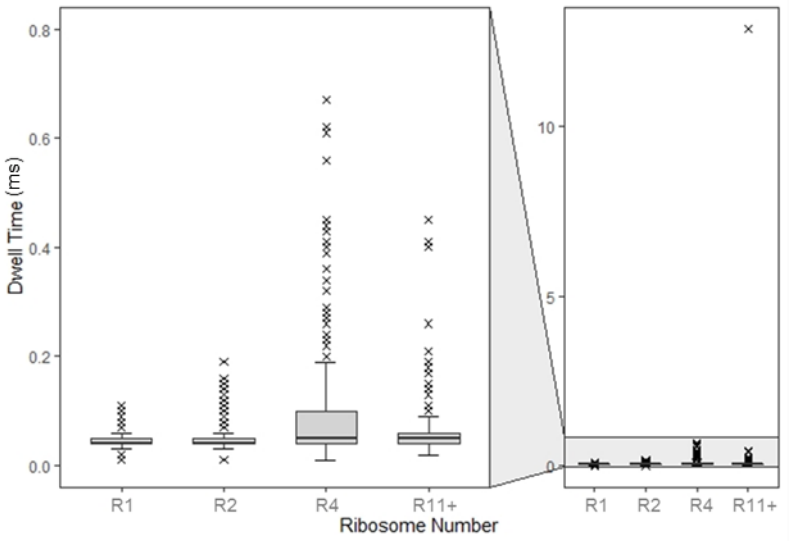

Figure 5.4 Boxplots showing the median value and lower quartile and upper quartile of dwell times for R1, R2, R4 and R11+ samples. The zoomed insert (left) shows dwell times from 0- 0.8ms, excluding the outlier of 12 ms from the R11+ sample. Each data represents >100 events.

5.3 Detection and Analysis of Ovary Ribosomes and Polysomes

Next, similar translocation experiments were performed on 80S ribosomes and mixed polysome fractions from *D. melanogaster* ovary cells, which were analysed using the same nanopore platform. Ovary polysomes are smaller than S2 embryo polysomes, and as such one would expect to see lower values for their peak amplitude as they traversed the nanopipette pore. Additionally, the ovary lysate are only collected in two fractions, 80S ribosomes (Or1) and a mixed polysome sample (Or2+), shown in Figure 5.5(a).

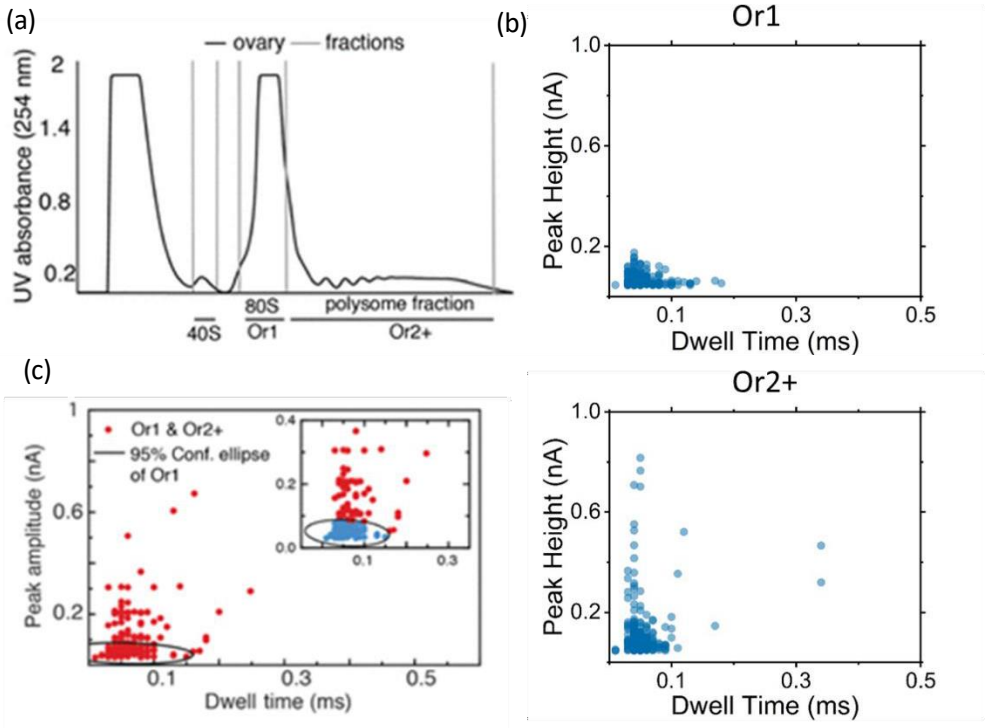

Figure 5.5 (a) UV (254 nm) profile for sucrose density gradient fractionation of *D. melanogaster* ovary lysate, with distinct fractions for 40S subunits, 80S ribosomes (Or1) and a mixed polysome fraction (Or2+). (b) Scatter plots of peak amplitude against dwell time for Or1 ribosomes and Or2+ polysome mixture. (c) Peak amplitude against dwell time data for the mixture of 80S ribosomes and polysomes from ovary lysate. Zoomed insert shows in blue events within the 95% confidence ellipse. Source: [81]. Mixed sample experiments were carried out by Mukhil Raveendran, School of Electronic and Electrical Engineering, University of Leeds.

As shown in Figure 5.5(b), the Or1 sample presents as a small cluster, indicating a homogeneous population, whereas the Or2+ sample, which is heterogeneous in nature shows a variety of different peak amplitudes. The peak amplitudes exhibited are smaller than that of R11+ samples from the embryonic lysate, which reached as high as 1.9 nA. This is expected as the ovary polysomes are lighter, and additionally demonstrates that peak amplitude is a reasonable measure to judge the size of the polysome fractions. The Or1 samples exhibited a mean dwell time of 0.04 ± 0.01 ms and a mean peak amplitude of 0.05 ± 0.01 nA, which are similar to the S2 80S means, albeit with a slightly lower mean peak amplitude. Whereas, the Or2+ samples had a mean dwell time of 0.04 ± 0.01 ms and a mean peak amplitude of 0.08 ± 0.01 nA. As expected, the peak amplitudes for the Or2+ sample was significantly different to that of the Or1+ sample ($P < 0.001$).

In our 2020 paper, myself and Raveendran *et al*. additionally demonstrated that it was possible to identify Or1 and Or2+ populations within a mixed sample. As demonstrated in Figure 5.5(c), the 95% confidence ellipse for Or1 events was used to identify Or1 events within the mixed sample. This demonstrates the possibility for nanopores to detect 80S ribosomes from polysomes within an unfractionated lysate [81]. These mixed sample experiments were performed by Mukhil Raveendran.

5.4 Signal Enhancement with Poly(ethylene) Glycol (PEG)

It has previously been reported that macromolecular crowding using polyethylene glycol (PEG) at a concentration of 50% (w/v) in the electrolyte bath enhances signal detection both in terms of the peak amplitude of each event, and in the ability to detect events previously unseen, thus increasing the number of events per trace. This was demonstrated for linear and circularised DNA plasmids, allowing differentiation between the two, a globular protein (β-galactosidase) and a filamentous protein (α-synuclein amyloid fibrils) [82].

In order to establish whether or not PEG could enhance the signal-to-noise ratio (SNR) of polysome detection to further differentiate between fractions, a nanopipette was filled with an Or2+ polysome mixture, and immersed in a bath of either 35K molecular weight (MW) PEG dissolved in 0.1M KCl to a final concentration of 50% (w/v), or 0.1M KCl alone. When the nanopipette and the bath were fitted with electrodes to complete the circuit, the current trace was recorded. Translocation events were observed as expected for the 0.1M KCl bath, however, upon moving the same pipette to a PEG bath, no events were observed (Figure 5.6(a)). This phenomenon was noted upon repeat experiments. Positive ion current rectification was also observed upon using the PEG bath (Figure 5.6(b)), which is consistent with previous reports [82], and is thought to be because PEG can intercalate cations [82, 83].

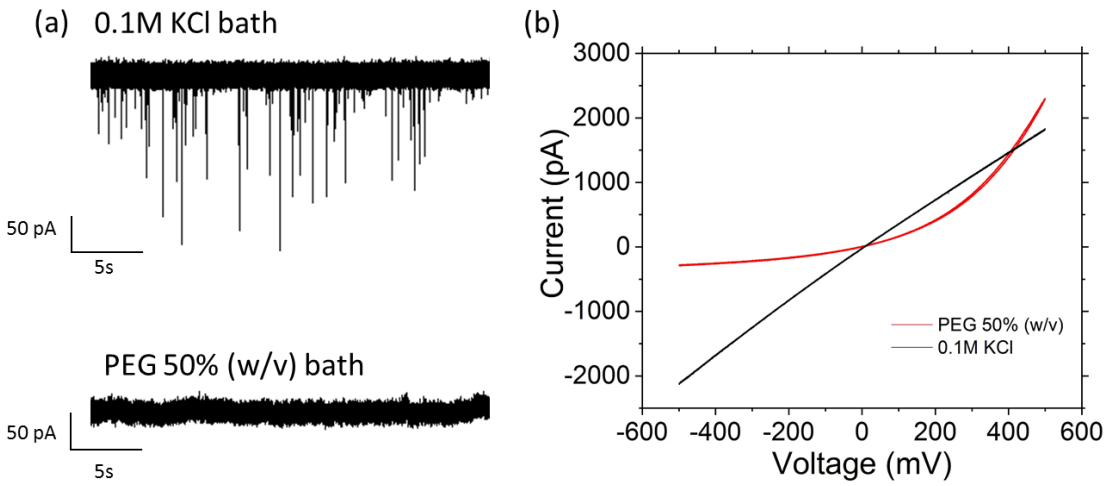

Figure 5.6 (a) Ion current traces for mixed O2+ polysome fractions in 0.1M KCl bath (top) and PEG 50% (w/v) bath (bottom). Translocation events are not observed when PEG is present in the bath. (b) Current-Voltage graph for nanopipettes immersed in 0.1M KCl only (black) and in PEG 50% (w/v) bath (red), indicating ion current rectification when immersed in PEG.

After establishing PEG could not be used in the bath solution to enhance the detection of Or2+ polysomes, the polysome solution was dissolved in either 4K or 8K PEG to a final concentration of either 1% (w/v) or 4% (w/v). It was hypothesised that this would slow down the translocation of the polysomes across the pore, and increase the dwell time, consistent with previous findings [84]. Over 100 events per sample were analysed and Or2+ polysomes in electrolyte only showed a mean dwell time of 0.05 ± 0.01 ms and a mean peak amplitude of 0.07 ± 0.01 nA. When the sample was dissolved in 1% (w/v) 4K PEG, it showed a mean dwell time of 0.08 ± 0.01 ms and a mean peak amplitude of 0.10 ± 0.01 nA, 4% (w/v) 4K PEG showed a mean dwell time of 0.13 ± 0.01 ms and a mean peak amplitude of 0.09 ± 0.01 nA, 1% (w/v) 8K PEG showed a mean dwell time of 0.14 ± 0.01 ms and a mean peak amplitude of 0.11 ± 0.01 nA and 4% 8K PEG showed a mean dwell time of 0.19 ± 0.01 ms and a mean peak amplitude of 0.11 ± 0.01 nA. Scatter plots demonstrating how the average peak amplitude and dwell time changes as a function of PEG MW and concentration are shown in figure 5.7. Figure 5.8(a-e) shows scatter plots of peak amplitude against dwell time for Or2+ ribosomes immersed in either electrolyte only, or 4K or 8K PEG at a final concentration of 1% (w/v) or 4% (w/v). The results indicate a higher concentration and a higher molecular weight of PEG increase the dwell time of the events, and increase the spread of dwell times, but the peak amplitude is unaffected.

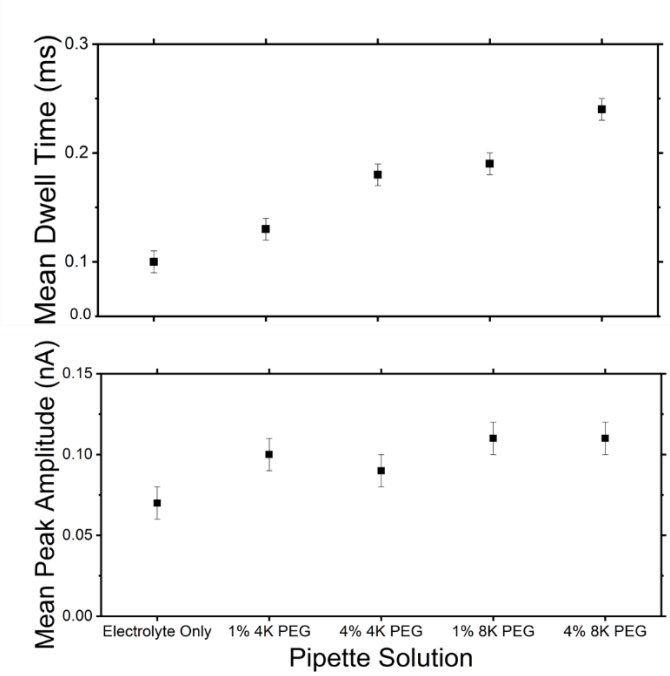

Figure 5.7 Average dwell time (top panel) and peak amplitude (bottom panel) for Or2+ sample with distinct concentration and molecular weight of PEG inside the nanopipette.

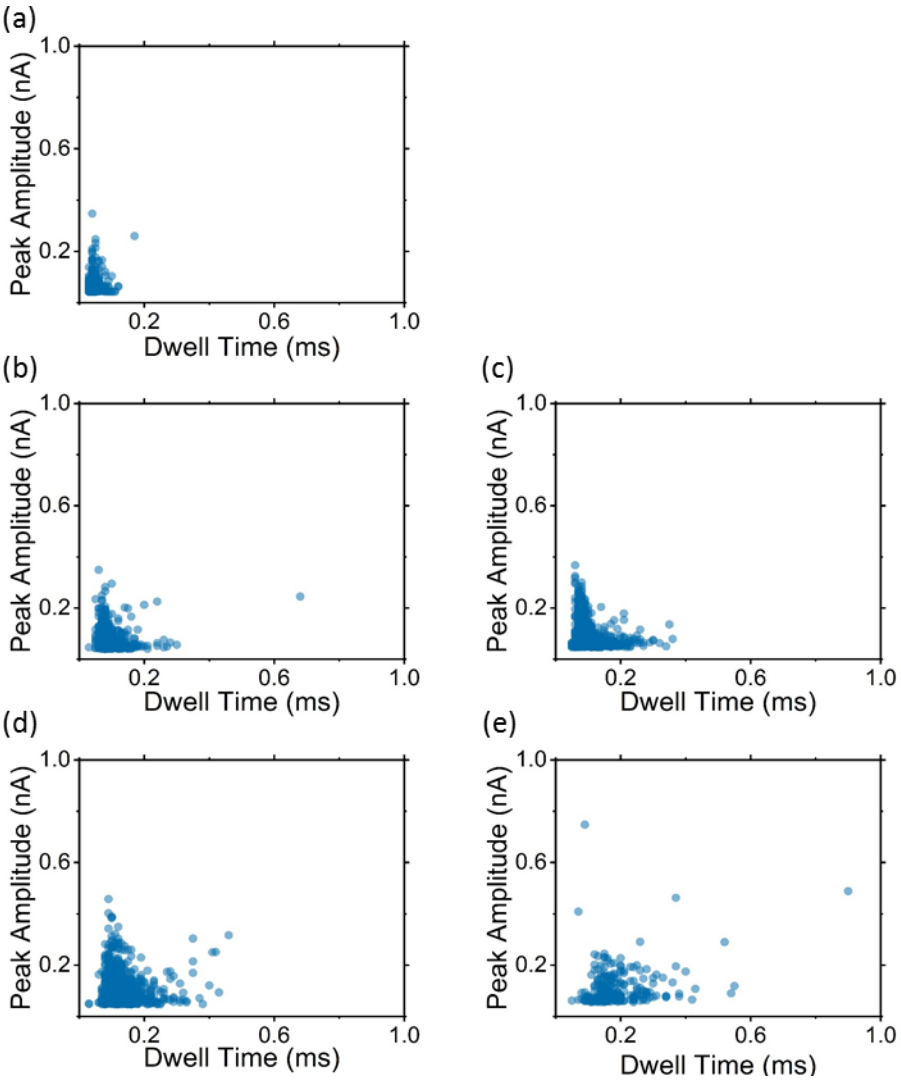

Figure 5.8 Peak amplitude against dwell time scatter plots for >100 events of Or2+ polysomes dissolved in (a) electrolyte only, (b) 1% 4K PEG, (c) 4% 4K PEG, (d) 1% 8K PEG, (e) 4% 8K PEG.

5.5 Conclusion

In this chapter, the successful detection of polysomes and ribosomes using a nanopipette was demonstrated. This was accomplished by using the characteristic ion current signature generated as they cross the nanopipette pore under a positive voltage. It was shown that the peak amplitude of the current blockade corresponded to ribosome number, with larger polysomes showing higher peak amplitudes. All translocation experiments were performed using volumes less than 10 μl, and a concentration of only 20 μg/ml.

Importantly, a significant difference was shown between the peak amplitude of 80S ribosomes and polysome fractions, and these findings were consistent across S2 embryo and ovary samples, and were corroborated by myself, Raveendran *et al.* in our 2020 paper [81]. These discoveries additionally enabled the generation of a fingerprint for 80S ribosomes and discrimination between the two in heterogeneous samples [81]. These results together evidence that nanopipettes could be used provide a quick-screening technique for detection of 80S ribosomes in a mixed lysate, and as a tool to detect and analyse ribosomes and polysomes.

Furthermore, preliminary evidence suggests that the addition of PEG to the ribosome or polysome solution within in the pipette increases the magnitude and distribution of the dwell time of translocations. This suggests that the dwell times observed after addition of PEG to the pipette solution could be used as an additional parameter for further differentiation between polysome fractions.

Chapter 6- Detection of Viral Genomic RNA

6.1 Introduction

In chapter 5, nanopipettes were used for the translocation and characterisation of ribosomes and polysomes. Given the successful demonstration of the use of nanopipettes within this chapter for the characterisation of biological entities composed of RNA and protein, this chapter moves forward in taking advantage of the platform to investigate whether it could be used to detect RNA, in the form of CHIKV(GAA) RNA which is a replication-deficient mutant of Chikungunya virus genomic RNA [85]. Viruses have major importance in clinical research, diagnosis, and therapeutics, as they are one of the main causes of infectious disease worldwide. Viruses are only capable of replicating within a host cell, and as such are termed obligate intracellular parasites. In general, they are composed of genetic material in the form of single- or double-stranded RNA or DNA inside a protein capsid. This capsid can be encapsulated by a lipid envelope in some viruses, termed envelope viruses [86].

Due to the integration of nanopipettes within a Scanning Ion Conductance Microscope (SICM), single molecules of CHIKV RNA could be delivered into the cytoplasm of a single cell. These experiments would simulate virus infection, and the cellular biological response to increasing number of viral genomes could be followed in experiments where one injects a single cell with the viral replicon, monitoring the number of RNA molecules injected into the cell using the modulations in the ion current trace generated when each molecule traverses the pore. If a version of the genome which expresses green fluorescent protein (GFP) is injected, one could follow GFP expression via fluorescence microscopy. If a successful infection proceeds, one would see an increase in GFP expression in the infected cell over a 24 hour period, which then may spread to other cells as they also become infected. The number of neighbouring cells infected when increasing numbers of viral RNA genomes are injected could be counted. Due to the ability to count the number of RNA molecules being injected using the ion current trace, one could count how many genomes are required for successful

infection and transmission. Therefore, the experiments in this chapter revolve around successful detection of CHIKV RNA using nanopipettes, as the ground work for further work in the future using SICM injection.

6.1.1 Chikungunya Virus (CHIKV)

CHIKV is a mosquito-borne virus from the Alphavirus genus, which causes debilitating joint pain, fever and skin rashes. The arthralgia associated with CHIKV infection can frequently become chronic and debilitating, lasting between months and years in up to 80% of patients, and can severely increase morbidity impacting upon quality of life [87, 88]. No specific anti-viral treatment or vaccine is available for CHIKV infection. CHIKV has a single stranded, positive sense genome composed of RNA which is around 11.8 kb in length. The genome encodes for 2 open reading frames (ORFs), with a 5' cap and a 3' polyadenylated tail. The first ORF encodes for 4 non-structural proteins, which make up the CHIKV replication complex. The second encodes for structural proteins from a sub-genomic RNA [89-91]. Single particle tracking studies have been used to elucidate CHIKV binding and entry, using multiple virions to infect multiple cells, using fluorescence markers to track single particles [88, 92]. Despite the existence of such single-particle tracking studies, to date there have been no single-cell single-particle infection studies of CHIKV. To truly investigate single particle single cell CHIKV infections, and the influence of increasing numbers of virus particles on progression and outcomes of the infection cycle, the introduction of a single viral particle into one single cell is required.

6.1.2 Scanning Ion Conductance Microscopy (SICM)

Scanning Ion Conductance Microscopy (SICM) is based on an electrode-fitted nanopipette probe, filled with electrolyte, immersed in a bath containing the sample of interest within an electrolyte solution. When a potential is applied between the pipette electrode and the bath (reference) electrode, an ion current will flow between the two. As the pipette reaches close proximity to the surface of the sample, the ion current will drop as there is less space for the

flow of ions to move (Fig 1). Because the ion current is therefore distance dependent, it can be used as a feedback mechanism to control the distance between the tip and the sample, and as the pipette follows the sample surface, the movement of the pipette in the *z*-direction is measured to recreate the topography of the sample [36].

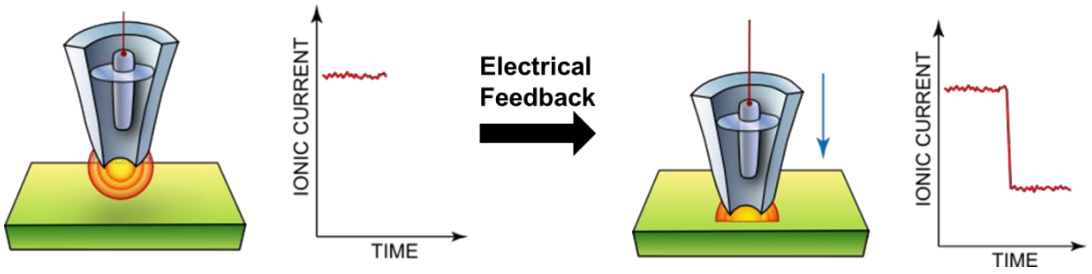

Figure 1-

Figure 6.1 An illustration of ionic current as a feedback measurement. As the nanopipette probe reaches the surface, a drop in ionic current is experienced, which can be used to position the pipette close to the surface of the sample of interest (Image created by David Liao).

Because SICM is a non-contact method used in solution, it is ideal for high-resolution imaging of live cells, and can recreate cellular topography in real-time [36]. Its force-free approach means that it can image delicate and intricate structures [36], such as neuronal networks and stereocilia [93], without the increased risk of sample damage or deformation experienced in techniques such as AFM, in which the sample encounters nonzero forces [94].

After imaging a cell, the nanopipette can be inserted through the cell membrane and used to either extract cytoplasmic contents, or inject materials. For example, Actis et al [95] demonstrated the use of this technology, whereby they used nanopipettes to sample small volumes, on the femtoliter scale, from living cells. The integration with SICM, enables the pipette to be precisely positioned above the cell membrane, following which the membrane is penetrated and cytoplasmic contents extracted by electrowetting. This process has minimal impact on cell viability, with a survival rate of >70%. To exhibit the applications of this approach, the authors extracted contents from HeLa cells expressing GFP, and generated cDNA copies of the RNA extracted, confirming the extraction of GFP mRNA using real-time PCR. In addition to this, the compatibility of the nanobiopsy technique with next-generation sequencing was illustrated by sequencing the cDNA copies of the mRNA extracted from HeLa cells.

Seger et al [96] used nanopipettes integrated with SICM to precisely position the pipette above mammalian cells, following which the tip was inserted in the cytoplasm and fluorescent dyes were injected, which was confirmed using fluorescence microscopy. The authors found that voltages between 10-20 V and an injection duration between 0.2 – 2 seconds provided a long-term viability of 70-100 %. Furthermore, 24 hours after the injection, cells were fluorescent and their morphology was normal. Additionally, after 27 hours, normal cell division was observed, producing fluorescent daughter cells with normal morphology. This study demonstrates that the technique is robust and minimally invasive.

6.1.3 Nanopore Detection of Viruses

There have been evidence of resistive pulse sensing of viruses and virus particles since the 1970s. For example, in 1977 DeBlois and Wesley [97] used polycarbonate pores, with a submicron diameter, to measure the sizes of several different type C oncornaviruses. They did this by comparing the pulse amplitudes of the viruses to those of standard latex beads. More recently, Zhou et al [98] characterised Hepatitis B virus capsids in conical solid-state nanopores, with a tip diameter of 40 nm. They were able to distinguish between capsids containing 90 and 120 capsid protein dimers, with the latter showing a larger dwell time on the resistive pulse.

In addition to the analysis of resistive pulse measurements of spherical viruses, there have been studies focusing on measuring rod-shaped viruses. For example Wu et al [99] used 25, 30 and 50 nm diameter solid-state nanopores to analysis the translocation of Tobacco Mosaic Virus. In this study they discovered that the virus must rotate in order to translocate the pore, after interaction with the surface of the pore, which influences the current signal recorded. Additionally, McMullen et al [100] studied the translocation of the stiff filamentous virus through 12-50 nm diameter solid-state nanopores. By observing the dwell time and peak amplitude of translocation blockades, they were able to distinguish between translocation events and collision events. The collisions of the virus with the nanopore resulted in events with a lower peak amplitude and dwell time to the translocation events.

6.1.4 Single Cell Virology Techniques

Viral infection has largely been examined using bulk infection techniques, which provides an overall view of infection outcomes, however does not show the heterogeneity between individual cells. For example, when using bulk infection techniques, the term multiplicity of infection (MOI) is used to describe the ratio of the number of infectious virions to the number of cells within a culture. However, this does not give the true picture of what is happening, as for example, a MOI of zero does not indicate no virus is present, it could be for example, the virus never came into contact with the target cells in order to be able to infect them. For example, adenoviral vectors diffuse very slowly, and so have a small particle to infectious unit ratio, and so have deemed to not be infectious in the past [101]. However, using a mathematical model based on Fick's Law of Diffusion and centrifugation, Nyberg-Hoffman et al [102] demonstrated that most adenovirus particles are actually capable of infection. As adenoviral particles diffuse very slowly in solution, they may not actually come into contact with the target cells, and increasing the MOI may not be effective [101].

Additionally, as a viral stock, or a stock solution of plasmids for transfection, is used to infect target cells, it may not give an accurate representation of true *in vivo* viral infection, where fewer viral particles would infect few numbers of cells. For example as few as two influenza A viruses have been shown to be necessary for successful infection [103]. Moreover, single cell analysis of virally infected cells have been shown to be heterogeneous. Russel et al [104] used single cell RNA sequencing to analyse the expression of influenza virus genes in mammalian cultured cells. The authors discovered that whilst measurements in bulk demonstrated an increase in viral mRNA over time, single cell sequencing revealed striking differences in the viral mRNA expressed in individual cells. In fact, around half of the infected cells failed to express any viral genes at all. Within the cells expressing all viral genes, heterogeneity was observed in the amounts of total viral mRNA between cells.

Single neurons have been selectively infected with a GFP-encoding rabies virus using a glass patch pipette filled with a solution the viral stock. To infect single cells, the pipette was

positioned above the neuron of interest, and a second, larger, micropipette was place opposite the pipette containing the virus. This second pipette was used as a ‘suction pipette’, to take away and leaking virus solution. When the pipette was brought into contact with the cell, the pipette pressure was slowly increased and once at the desired level was left for 30-50 minutes. Following this the pipette was retracted and the cells were incubated. Firstly, single neurons were infected and GFP expression was detected 16-25 hours post infection, with a success rate of 83% and a selectivity of 100%. Following infection, its spread from the original infected neurons was monitored, the cell culture being observed ever 2-4 hours. The number of GFP expressing cells was recorded over time, and new bursts of cells being infected were observed after around 31 and 41 hours post original infection, indicating first and second order infections. Next, the authors successfully selectively infected a single neurons in tissue slice, and were able to observe transynaptic fluorescence in 60% of the slices.

In 2017, Schubert and co-workers [105] developed a virus stamping technique, which involved bringing a blunt glass pipette tip with an attached virus in contact with a single cell. The glass pipette was flame blunted, following which it was functionalised with N^1-(3-trimethoxysilylpropyl)diethylenetriamine30 (AEEA), a cationic polymer which would electrostatically bind to either lenti or rabies viruses which were coated in a negatively charged viral glycoprotein, vesicular stomatitis virus envelope glycoprotein (VSVG). The authors held the pipette tip into contact with a cell body for 1 min, and discovered that the virus particles had been discharged from the pipette tip at this location, by observing the pipette tip under SEM. In order to test whether single cells that had been stamped with a virus had been successfully infected, viruses encoding the fluorescent proteins tdTomato or GFP, and stamping resulted in fluorescence expression after 24 hours. Following this, two different adjacent neurons were stamped with different viruses, one encoding tdTomato, the other GFP, and consequently each neuron exhibited bright fluorescence, but with different coloured fluorophores. Next single neurons were stamped with a tip with both GFP and tdTomato expressing viruses, and co-infection was observed with the expression of both fluorophores.

Envelope viruses that were not coated with VSVG, as well as non-envelope viruses were also investigated. Individual neurons were stamped with VSVG coated rabies viruses which

encoded for GFP. After 48 hours, these cells were then stamped with herpes simplex viruses (HSVs) which were not coated with VSVG and encoded for mCherry. 52 hours after the first stamping, the cells were observed to be expressing both GFP and mCherry. Next, individual neurons were stamped concurrently with non-VSVG coated rabies viruses expressing GFP and non-VSVG coated HSVs encoding tdTomato, and expression of both fluorophores were observed at day 3, 5 and 7 after initial stamping. Finally, individual neurons were stamped with non-enveloped adeno-associated viruses (AAVs) which encoded for either mRuby or GCaMP6s, and expression of both fluorophores was detected 14 days after initial stamping.

The authors furthered the approach of single cell stamping in order to be able to infect single cells deeper within a tissue, using a technique they termed shielded virus stamping. Instead of binding the viruses to a blunted glass pipette, they were bound onto magnetic nanoparticles. The virus-bound magnetic nanoparticles were then put into a glass pipette in order to shield them and prevent non-specific infection. After positioning the pipette at the surface of the target cell, an electromagnet in line with the pipette was switched on, resulting in the virus-bound magnetic nanoparticles coming into contact with the target cell membrane. Shielded virus stamping was accomplished on a cultured cell of interest by positioning the pipette tip adjacent to it, and switching on the electromagnet for 3-5 minutes, following which the magnet was switched off and the pipette withdrawn. This was achieved on pre-selected cells that expressed GFP, and the successful infection was demonstrated by expression of mCherry. Following this, the method was investigated within tissue, *in vivo*, on neurons in the visual cortex of an anesthetized mouse, around 130- 300 μm below the surface of the brain. The pipette was filled with Alexa 594 dye and magnetic nanoparticles with VSVG-coated lenti viruses encoding GFP. Fluorescent dye was discharged from the pipette, filling the extracellular space in order to expose the cell bodies of neurons within that location, visualised as dark shadows using a two-photon microscope. The tip of the pipette was then position at the cell body of an individual neuron, the electromagnet was switched on for 3-5 minutes, and the nanoparticles were brought into physical contact with the cell membrane. Following this, the pipette was withdrawn, and after 1-4 days post-virus stamping the target cell expressed GFP, showing successful infection. The magnetic field was not shown to significantly affect the health of the cells.

The shielded stamping was also executed in human brain organoids, which were developed from induced human pluripotent stem cells, using VSVG-coated rabies viruses which encoded for GFP. Single cells were targeted 50-150 μm below the surface of the brain organoid, using the same technique noted above. After shielded stamping was carried out, the organoids were incubated, and single GFP-expressing cells were observed after 3-5 days. The authors additionally investigated as to whether the approach could be used to infect specific pre-selected cells within a tissue sample. To achieve this, brain organised were sparsely transfected with plasmids which encoded for tdTomato, and shielded virus stamping using VSVG-coated, GFP encoding rabies viruses was carried out on single tdTomato expressing cells. After 3-5 days, individual cells which expressed both GFP and tdTomato were observed, demonstrating successful infection.

FluidFM, a technique based on Atomic Force Microscopy (AFM), has been used to infect single cells with the vaccinia virus (VACV) [106]. AFM is a form of scanning probe microscopy, which principally consists of a cantilever, a laser, an optical beam detector (OBD) and a piezoelectric positioner. The tip at the end of the cantilever is used as the probe and it responds to forces between the tip and the sample. AFM is chiefly used as an imaging technique, whereby the tip scans the sample, with either the sample or the cantilever being moved relative to the other by the piezoelectric positioners. A laser is beamed onto and reflected off the back of the cantilever onto the OBD, which is used as feedback to measure the deflection of the cantilever which can then be used to generate the topography of the sample [107]. In FluidFM, a cantilever with a nanoscale tip containing a microchannel is attached to a pressure controller, allowing pressure driven liquid intake or expulsion of volumes smaller than a femtoliter. Fluid FM retains all the strengths of AFM, in that it can use force-feedback to precisely position the tip at the surface of the cell of interest, with a nanometer range of positional control. Furthermore, as the FluidFM set-up additionally utilises an optical microscope, experiments can be monitored optically in real-time [106, 108].

Using FluidFm, Stiefel et al [106] depositied VACV particles onto single cells, to investigate the infection of single cells by both single and multiple VACV viral particles. The authors constructed a fluorescently labelled VACV, which had an mCherry labelled VACV core

protein A5, and which began to express Enhanced GFP (EGFP) after the virus had entered host cells. During the early stages of infection, the mCherry signal could be monitored to assess whether the deposited VACV viral particles had bound to the host cell and been internalised. Loss of fluorescence at the cell surface can be taken to be internalisation of the virus into the cell. If a virus particle successfully entered a cell, and underwent early or late gene expression, this could be observed by the expression of EGFP. Furthermore, mCherry was also able to mark viral assembly later after successful infection, because it would then be incorporated into the new assembling VACV viral particles. This in total can be used to monitor which virus particles undergo successful infection, which are not, and at which point in the virus lifecycle they are impeded.

The authors experimented with different pressures applied to the cantilever, whilst observing the motion of the viruses in the channel using fluorescent microscopy. They determined that the application of 5 mbar of pressure was a reproducible method to release a single virus from the cantilever. Subsequently, the catilever was positioned near the cell of choice, and using force-feedback was brought into contact with its surface. After application of 5 mbar pressure to the cantilever, a single virus was released, and the pressure and the cantilever were removed. After deposition of single viruses on to a cell, the movement and action of the viruses were monitored using fluorescence. For example, three viruses were placed on a cell, and an internalisation event was observed for one after 55 minutes, the next after 2.5 hours, and the third remained on the cell surface. The cell started expressing visible levels of EGFP after six hours, however, it did not at any point exhibit detectable levels of mCherry which demonstrates the virus was blocked before late gene expression, and viral progeny were not assembled.

A successful replication cycle was denoted by the mCherry fluorescence of the virus disappearing at the cell surface as the virus is internalised, the detection of EGFP around six hours later, and then a detectable increase in EGFP expression five hours later, which is associated with late viral gene expression. Shortly after this, mCherry labelled virus particles appear, demonstrating successful assembly. Following assembly, the spread of the virus to surrounding cells can be observed by the appearance of EGFP expression. To monitor at which stage of the lifecycle VACV particles got blocked, single viruses were placed onto

single host cells and observed for 24 hours. 73 single virus, single cell interactions were monitored, and it was discovered that whilst 48% of the VACV could enter cells, 9.6% of them induced early gene expression, and under 2% completed the lifecycle and underwent assembly.

The results of this paper show an important difference in infection outcomes between bulk infection and single particle infection. It is therefore crucial to perform single particle single cell studies in the future in order to gain a perspective of how an infection would progress *in vivo,* where high quantities of virus particles infecting each single cell as simulated in bulk infection is unlikely, and additionally to gain a perspective on how virus load affects the progression of a viral infection.

6.2 Single Molecule Detection of Viral Genomic RNA

6.2.1 Introduction

CHIKV(GAA) genomic RNA was diluted in either 0.1M KCl with 6 mM $MgCl_2$, PBS-TWEEN 20, or 0.1M KCl with 1 x TE buffer, and at different concentrations of RNA: 300 pM, 30 pM and 3 pM, to find the optimum conditions. The conditions which generated detectable and a suitable quantity of events in the ion current trace with a stable baseline were RNA viral replicon diluted in 0.1M KCl with 1 x TE buffer to a final concentration of 30 pM. The RNA traverses the nanopipette pore under a negative voltage bias, and events are seen as downwards peaks, amplifying the ionic current rather than restricting it, which indicates a conductive pulse, rather than a resistive pulse. This is illustrated in figure 6.2 which shows a 2 minute trace both in the presence and absence of CHIKV viral replicon. The RNA molecules are negatively charged and so the negative bias will have an electrophoretic effect on the viral replicons, causing them to exit the nanopipette pore, and as they are traversing the pore, they will attract K^+ ions within the tip and thus cause an increase in current [64].

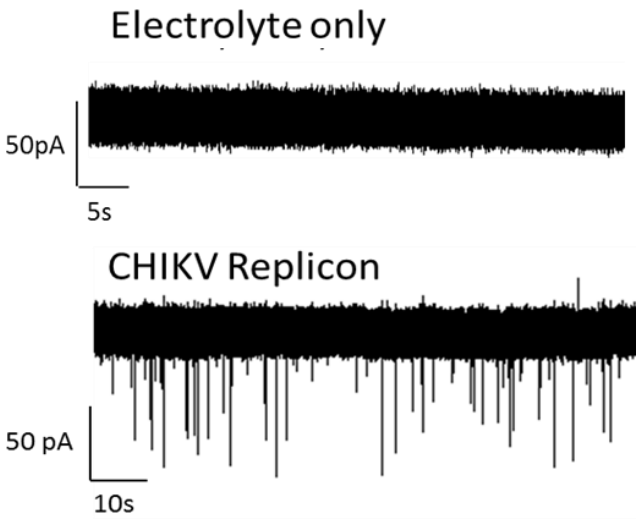

Figure 6.2 Ion current traces in electrolyte only (top) and in the presence of CHIV replicon (bottom). In the presence of CHIV replicon RNA, downwards peaks in the ion current are observed, representing one replicon passing through the nanopipette pore, and temporarily amplifying the ion current.

6.2.2 Detection of CHIKV RNA

Figure 6.3 shows a scatter plot of peak amplitude against dwell time, yielded from events taken from a 2 minute trace of >100 events at -400mV. Nearly all of the events are within a tight cluster, which indicates a homogeneous population, and that the nanopore is only allowing one molecule to traverse the pore at a time, as due to the nature of the conductive pulse, one would expect that if more than one RNA molecule traversed at once, this would cause the amplification in the ion current to be higher, and all peak heights in Figure 6.3 are very close to each other. There are 3 events within the scatter plot that have a longer dwell time, and as their peak amplitudes are consistent with the other events, one would expect this to be due to them getting lodged in the nanopipette tip for a short time before passing through, rather than multiple molecules traversing at the same time

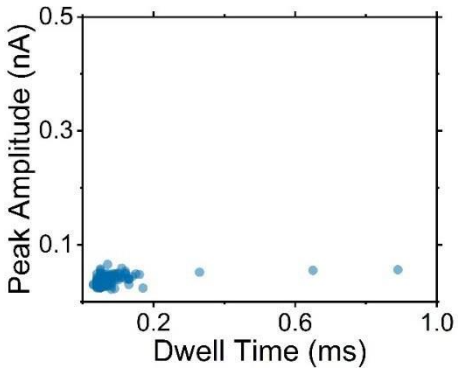

Figure 6.3 Scatter plot of peak amplitude against dwell time for the viral RNA replicon from a 2 minute trace, using >100 events.

To facilitate future experiments performing SICM injections of increasing numbers of viral RNA, experiments were performed at increasing concentrations of CHIKV replicon at -400mV, in order to determine how many replicons could traverse the pore per minute at differing concentrations. The RNA was diluted with 0.1M KCl with 1 x TE buffer to form dilutions of 1 in 10, 1 in 50 and 1 in 100, resulting in final concentrations of 30 pM, 6pM and 3pM. The 1 in 10 dilution resulted in an average of 48 events per minute, the 1 in 50 dilution resulted in an average of 13 events per minute, and the 1 in 100 dilution resulted in an average of 3 events per minute. Figure 6.4 shows a 60 second trace for each dilution, indicating the decreasing number of events as the concentration decreases. This shows that it is possible to use dilutions of the CHIKV replicon to deliver small numbers of viral replicon, allowing some precision and control over the number of replicons injected.

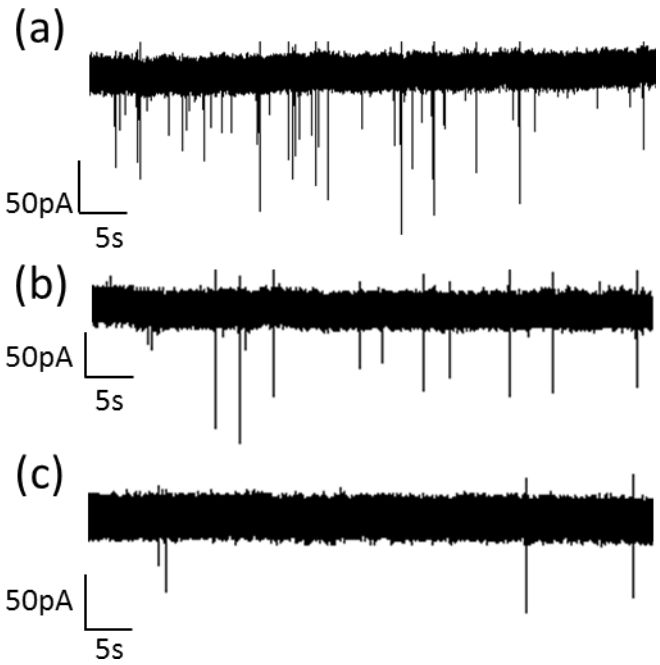

Figure 6.4 60 second traces showing events detected for (a) 1 in 10, (b) 1 in 50 and (c) 1 in 100 dilutions of CHIKV replicon.

6.3 Conclusion

The results presented in this chapter show the suitability for the nanopore platform to detect and analyse the Chikungunya CHIKV-nsP4-GAA-FLuc-SGR RNA viral replicon. Specifically, when observing the ion current characteristics of the translocation events, the dwell times and peak amplitudes of the majority of events were in a single tight cluster, which confirms a homogeneous population. These show that the CHIKV viral replicons have a predictable ion current signature which can be used for its identification. Furthermore, the similarity of peak heights shows that the nanopipette only allowed one RNA molecule through the pore at a time.

Additionally, further experiments using increasing dilutions of CHIKV replicon demonstrated that the replicon could still be detected at concentrations as low as 3 pM. Furthermore, such dilutions provide the ability to have a higher level of control of the number of replicons released by the nanopipette, by lowering the frequency of events without impeding successful detection. For example, a concentration of 3 pM elicited three events per minute, which confirms the ability of the platform to be used in scenarios when a controlled number of replicons are required.

Chapter 7- Conclusions and Future Developments

7.1 Conclusions

Nanopores have been widely used to analyse biological molecules and single entities, and are becoming increasingly popular as a platform as a sensitive means of biomolecular detection and analysis. This has been evidenced by the wide-reaching application of nanopore-based resistive pulse sensing of many biomolecules, from proteins to nucleic acids. Furthermore, the groundbreaking success in the nanopore sequencing of DNA, leading to the commercialisation of the Oxford Nanopore MinION demonstrates the ability of this field to revolutionise the landscape of biomolecular analysis.

In recent years, the ability of nanopores to perform experiments with single-molecule precision has been expanded to the domain of RNA analysis, specifically having been extensively used for RNA sequencing. Furthermore, nanopores have been applied to analysing the structure of RNA and RNA complexes. Despite this advancement, previous literature had not tapped the potential of nanopores as a bioanalytical tool for studying ribosomes and polysomes. Two studies had used nanopores to detect and voltage gate either bacterial ribosomes or 50S subunits [5, 80], however a comprehensive analysis of individual ribosomes and polysomes had not been performed. In Chapter 5, and the paper I published as joint first author with Mukhil Raveendran [81], the potential of nanopipettes was expanded to differentiate between 80S ribosomes and polysomes, across different cell types.

The results presented in chapter 5 evidence that quartz glass nanopipettes can be used to discriminate between eukaryotic ribosomes and polysomes, with the peak amplitude of the translocation events increasing with polysome size. Furthermore, a significant difference was found between the peak amplitude of events generated by heavy polysomes with more than 11 ribosomes and lighter polysomes with approximately 4 ribosomes and 80S ribosomes,

enabling discrimination between the three. Furthering this research, myself, Raveendran *et al.* found a significant different between polysomes with more than 11, 4, 2 ribosomes per mRNA [81].

These results together establish the use of nanopores as a screening technique for polysome samples and provide a firm foundation for the use of nanopipettes to discriminate between polysome fractions, showing evidence for the suitability of the platform to detect them. As actively translating ribosomes are widely regarded in the literature as “heavy” ribosomes with 3 or more ribosomes bound per mRNA [66, 68], these experiments could provide the groundwork for future work using the nanopore platform as a complement to sucrose density ultracentrifugation, separating heavy polysomes from light polysomes.

The great benefit to the approach outlined in this report, is that one can detect the ribosomes and polysome fractions on a single-entity level, which enables us to see heterogeneity within samples that is unseen in molecular analysis and enables us to perform molecular counts. Furthermore, all nanopore experiments were performed under physiological conditions and thus should not interfere with the integrity of the samples. Additionally these experiments were performed with only small volumes of analyte (<10 μl) and at low concentrations (20μg/ml), and each individual ion current trace was recorded for only 2 minutes. This is hugely beneficial when samples are rare or precious, as is the case with *D. melanogaster* samples, where dissection to prepare enough sample for sucrose density ultracentrifugation takes a matter of weeks. Thus, one could envisage, with further differentiation of the polysome fractions, a nanopore approach to be an ideal quick screening technique.

The results presented in Chapter 6 provide further evidence for the successful application of nanopores to the field of RNA biology, demonstrating the successful detection of the Chikungunya CHIKV-nsP4-GAA-FLuc-SGR RNA viral replicon using resistive pulse sensing. Furthermore, the dilution studies presented at the end of the chapter show the potential for the control of the number of viral genomes released by the nanopipette, providing the groundwork for controlled delivery of single viral genomes.

7.2 Future Perspectives

The experiments outlined in Chapter 5 and my 2020 paper with Mukhil Raveendran [81] underpin the groundwork for the nanopipette platform to detect and analyse 80S ribosomes and fractions of polysomes differing in the number of ribosomes bound per mRNA. Furthermore, by using PEG within the pipette in Chapter 5, the dwell time increased, offering a further parameter for detection and analysis in the future. One can foresee with this increased sensitivity the ability to fully map and discriminate between the polysome fractions in the future. This could result in the ability of nanopores to be used to separate polysome fractions from mixed lysate as an alternative to sucrose density ultracentrifugation, or as a complement to it.

Moreover, the idea of ribosomes as a homogenous population has rapidly been shifting, with discoveries of ribosome heterogeneity and specialisation [109]. In their 2022 paper, Shiao [110] envisaged nanopore technology as a future means of capturing individual ribosomes for further downstream analysis, by recognition of their characteristic ion signature as they traverse the pore. Further, improvements to the sensitivity of detection could aid the structural analysis of ribosomes and polysomes, using the ion current signature characteristics.

Further future work could involve further experiments with different concentrations and molecular weights of PEG to provide better resolution. Specifically, members of the Bioelectronics group have demonstrated in results currently in pre-print [111] that that increasing the molecular weight of PEG present in the electrolyte bath increases the magnitude of both the current peak amplitude and dwell time of translocation events, with the highest signal to noise ratio being exhibited by 35K PEG. Therefore, future experiments could be performed to assess whether 35K PEG has a similar effect when present within the pipette, in order to better resolve between polysome fractions.

In addition, the type of electrolyte used in a nanopore experiment can additionally aid greater resolution. When the size cation in the electrolyte is decreased, from K^+ to Na^+ to Li^+, the

dwell time increases for both double stranded and single stranded DNA, due to increased strength in their binding to the DNA. This slowing down of the translocation time enables better resolution [112]. Furthermore, the aforementioned preprint results from the Bioelectronics group have demonstrated that the signal enhancement provided by PEG when present in the electrolyte bath is due to a cooperative effect between the electrolyte used and PEG. CsBr was discovered to be the optimal electrolyte for the detection and analysis of double stranded DNA with high signal to noise ratio [111]. One could envisage future experiments investigating the effect of different sized cations and anions in the electrolytes on the signal to noise ratio in combination of increasing molecular weight PEG.

In a heterogeneous sample, even with small nanopore sizes, it can be difficult to resolve individual analytes, especially when they are similar to each other, as it requires a distinct current blockade for each sample, with no overlap in dwell time and peak amplitude. Therefore, machine learning can be employed to overcome this challenge and to accurately distinguish between samples in a heterogeneous mixture. A shapelet-based algorithm has been demonstrated to be able to detect oligonucleotide sequences GAAA and AAAA, which would normally be very difficult to differentiate between using traditional methods [113] Additionally, Henley *et al.* used machine learning to identify the characteristic ion current blockades from different tRNA molecules, with 88% accuracy [78]. Therefore, a machine learning approach could be employed in future to better resolve between different polysome fractions.

Furthermore, the results presented in Chapter 6 demonstrating the successful detection of CHIV RNA were performed with a low sample volume and concentration (<10 μl at 30pM), at the single molecule level, and within cell culture medium. This is advantageous, because it provides the groundwork for future experiments where one could inject single cells with different numbers of viral genomes, using the number of ion current blockades to count the viral particles injected. Furthermore, the dilution studies presented at the end of the chapter show the potential for the control of the number of viral genomes injected per cell. This is because with a low frequency of events, such as the 3 events per minute demonstrated by the 3 pM sample, there is a significant gap in time between translocations, therefore one could

stop the voltage and therefore the translocations after a predetermined number of events have been observed on the ion current trace.

The work in chapter 6 could be enhanced further in future, in order to have precise control over the number of viral replicons injected into the cell and the timing of injections. This could be achieved by using voltages of alternate polarities, where a negative voltage is applied to allow one molecule to be released, following which the polarity of the voltage is switched for a defined time [114]. This data could be used to elucidate how the viral load affects viral infection by following biological markers within the infected cells, as discussed in chapter 6.

Chapter 8- References

[1] L. Reynaud, A. Bouchet-Spinelli, C. Raillon, and A. Buhot, "Sensing with Nanopores and Aptamers: A Way Forward," *Sensors*, vol. 20, 2020.

[2] L. Xue, H. Yamazaki, R. Ren, M. Wanunu, A. P. Ivanov, and J. B. Edel, "Solid-state nanopore sensors," *Nature Reviews Materials*, vol. 5, pp. 931-951, 2020/12/01 2020.

[3] F. Haque, J. Li, H.-C. Wu, X.-J. Liang, and P. Guo, "Solid-state and biological nanopore for real-time sensing of single chemical and sequencing of DNA," *Nano Today*, vol. 8, pp. 56-74, 2013/02/01/ 2013.

[4] M. Muthukumar, C. Plesa, and C. Dekker, "Single-molecule sensing with nanopores," *Physics Today*, vol. 68, pp. 40-46, 2015.

[5] M. I. Rudenko, M. R. Holmes, D. N. Ermolenko, E. J. Lunt, S. Gerhardt, H. F. Noller, *et al.*, "Controlled gating and electrical detection of single 50S ribosomal subunits through a solid-state nanopore in a microfluidic chip," *Biosensors and Bioelectronics*, vol. 29, pp. 34-39, 2011/11/15/ 2011.

[6] Y.-L. Ying, J. Wang, A. R. Leach, Y. Jiang, R. Gao, C. Xu, *et al.*, "Single-entity electrochemistry at confined sensing interfaces," *SCIENCE CHINA Chemistry*, vol. 63, p. 589, 2020.

[7] J. D. Spitzberg, A. Zrehen, X. F. van Kooten, and A. Meller, "Plasmonic-Nanopore Biosensors for Superior Single-Molecule Detection," *Advanced Materials*, vol. 31, p. 1900422, 2019.

[8] Y. Song, J. Zhang, and D. Li, "Microfluidic and nanofluidic resistive pulse sensing: a review," *Micromachines*, vol. 8, p. 204, 2017.

[9] J. Menestrina, C. Yang, M. Schiel, I. Vlassiouk, and Z. S. Siwy, "Charged Particles Modulate Local Ionic Concentrations and Cause Formation of Positive Peaks in Resistive-Pulse-Based Detection," *The Journal of Physical Chemistry C,* vol. 118, pp. 2391-2398, 2014/02/06 2014.

[10] W. Shi, A. K. Friedman, and L. A. Baker, "Nanopore Sensing," *Analytical Chemistry,* vol. 89, pp. 157-188, 2017/01/03 2017.

[11] R. Maugi, P. Hauer, J. Bowen, E. Ashman, E. Hunsicker, and M. Platt, "A methodology for characterising nanoparticle size and shape using nanopores," *Nanoscale,* vol. 12, pp. 262-270, 2020.

[12] E. L. C. J. Blundell, L. J. Mayne, E. R. Billinge, and M. Platt, "Emergence of tunable resistive pulse sensing as a biosensor," *Analytical Methods,* vol. 7, pp. 7055-7066, 2015.

[13] H. Bayley and C. R. Martin, "Resistive-Pulse SensingFrom Microbes to Molecules," *Chemical Reviews,* vol. 100, pp. 2575-2594, 2000/07/01 2000.

[14] L. Luo, S. R. German, W.-J. Lan, D. A. Holden, T. L. Mega, and H. S. White, "Resistive-Pulse Analysis of Nanoparticles," *Annual Review of Analytical Chemistry,* vol. 7, pp. 513-535, 2014.

[15] W. H. Coulter, "Means for counting particles suspended in a fluid," ed: Google Patents, 1953.

[16] Y. Wang, D. Wang, and M. V. Mirkin, "Resistive-pulse and rectification sensing with glass and carbon nanopipettes," *Proceedings of the Royal Society A: Mathematical, Physical and Engineering Sciences,* vol. 473, p. 20160931, 2017.

[17] J. J. Kasianowicz, E. Brandin, D. Branton, and D. W. Deamer, "Characterization of individual polynucleotide molecules using a membrane channel," *Proceedings of the National Academy of Sciences of the United States of America,* vol. 93, pp. 13770-13773, 1996.

[18] M. Jain, H. E. Olsen, B. Paten, and M. Akeson, "The Oxford Nanopore MinION: delivery of nanopore sequencing to the genomics community," *Genome Biology,* vol. 17, p. 239, 2016/11/25 2016.

[19] D. Deamer, M. Akeson, and D. Branton, "Three decades of nanopore sequencing," *Nature Biotechnology,* vol. 34, pp. 518-524, 2016/05/01 2016.

[20] D. J. Burgess, "Expanding applications for nanopore sequencing," *Nature Reviews Genetics,* vol. 21, pp. 67-67, 2020/02/01 2020.

[21] L. M. Petersen, I. W. Martin, W. E. Moschetti, C. M. Kershaw, and G. J. Tsongalis, "Third-Generation Sequencing in the Clinical Laboratory: Exploring the Advantages and Challenges of Nanopore Sequencing," *Journal of Clinical Microbiology,* vol. 58, pp. e01315-19, 2019.

[22] N. Varongchayakul, J. Song, A. Meller, and M. W. Grinstaff, "Single-molecule protein sensing in a nanopore: a tutorial," *Chemical Society reviews,* vol. 47, pp. 8512-8524, 2018.

[23] E. C. Yusko, B. R. Bruhn, O. M. Eggenberger, J. Houghtaling, R. C. Rollings, N. C. Walsh, *et al.*, "Real-time shape approximation and fingerprinting of single proteins using a nanopore," *Nature Nanotechnology,* vol. 12, pp. 360-367, 2017/04/01 2017.

[24] S. Zernia, N. J. van der Heide, N. S. Galenkamp, G. Gouridis, and G. Maglia, "Current Blockades of Proteins inside Nanopores for Real-Time Metabolome Analysis," *ACS Nano,* vol. 14, pp. 2296-2307, 2020/02/25 2020.

[25] N. S. Galenkamp, M. Soskine, J. Hermans, C. Wloka, and G. Maglia, "Direct electrical quantification of glucose and asparagine from bodily fluids using nanopores," *Nature Communications,* vol. 9, p. 4085, 2018/10/05 2018.

[26] C. Cao and Y.-T. Long, "Biological Nanopores: Confined Spaces for Electrochemical Single-Molecule Analysis," *Accounts of Chemical Research,* vol. 51, pp. 331-341, 2018/02/20 2018.

[27] L. Ma and S. L. Cockroft, "Biological Nanopores for Single-Molecule Biophysics," *ChemBioChem,* vol. 11, pp. 25-34, 2010/01/04 2010.

[28] C. G. Brown and J. Clarke, "Nanopore development at Oxford Nanopore," *Nature Biotechnology,* vol. 34, pp. 810-811, 2016/08/01 2016.

[29] Q. Chen and Z. Liu, "Fabrication and Applications of Solid-State Nanopores," *Sensors,* vol. 19, p. 1886, 2019.

[30] J. Li, D. Stein, C. McMullan, D. Branton, M. J. Aziz, and J. A. Golovchenko, "Ion-beam sculpting at nanometre length scales," *Nature,* vol. 412, pp. 166-169, 2001/07/01 2001.

[31] Z. Tang, D. Zhang, W. Cui, H. Zhang, W. Pang, and X. Duan, "Fabrications, Applications and Challenges of Solid-State Nanopores: A Mini Review," *Nanomaterials and Nanotechnology,* vol. 6, p. 35, 2016/01/01 2016.

[32] K. Lee, K.-B. Park, H.-J. Kim, J.-S. Yu, H. Chae, H.-M. Kim, *et al.*, "Recent Progress in Solid-State Nanopores," *Advanced Materials,* vol. 30, p. 1704680, 2018/10/01 2018.

[33] J. Edel and T. Albrecht, *Engineered Nanopores for Bioanalytical Applications: A Volume in Micro and Nano Technologies*, 2013.

[34] Z. Yuan, C. Wang, X. Yi, Z. Ni, Y. Chen, and T. Li, "Solid-State Nanopore," *Nanoscale Research Letters,* vol. 13, p. 56, 2018/02/20 2018.

[35] Y. Zhou, M. Saito, T. Miyamoto, P. Novak, A. I. Shevchuk, Y. E. Korchev, *et al.*, "Nanoscale Imaging of Primary Cilia with Scanning Ion Conductance Microscopy," *Analytical Chemistry,* vol. 90, pp. 2891-2895, 2018/02/20 2018.

[36] C.-C. Chen, Y. Zhou, and L. A. Baker, "Scanning Ion Conductance Microscopy," *Annual Review of Analytical Chemistry,* vol. 5, pp. 207-228, 2012.

[37] M. Simonis, W. Hübner, A. Wilking, T. Huser, and S. Hennig, "Survival rate of eukaryotic cells following electrophoretic nanoinjection," *Scientific Reports,* vol. 7, p. 41277, 2017/01/25 2017.

[38] S. Hennig, S. van de Linde, M. Lummer, M. Simonis, T. Huser, and M. Sauer, "Instant Live-Cell Super-Resolution Imaging of Cellular Structures by Nanoinjection of Fluorescent Probes," *Nano Letters,* vol. 15, pp. 1374-1381, 2015/02/11 2015.

[39] J. Lv, R.-C. Qian, Y.-X. Hu, S.-C. Liu, Y. Cao, Y.-J. Zheng, *et al.*, "A precise pointing nanopipette for single-cell imaging via electroosmotic injection," *Chemical Communications,* vol. 52, pp. 13909-13911, 2016.

[40] C. Chau, P. Actis, and E. Hewitt, "Methods for protein delivery into cells: from current approaches to future perspectives," *Biochemical Society Transactions,* vol. 48, pp. 357-365, 2020.

[41] J. Y. Sze, S. Kumar, A. P. Ivanov, S. H. Oh, and J. B. Edel, "Fine tuning of nanopipettes using atomic layer deposition for single molecule sensing," *Analyst,* vol. 140, pp. 4828-34, Jul 21 2015.

[42] X. Xu, C. Li, Y. Zhou, and Y. Jin, "Controllable Shrinking of Glass Capillary Nanopores Down to sub-10 nm by Wet-Chemical Silanization for Signal-Enhanced DNA Translocation," *ACS Sensors,* vol. 2, pp. 1452-1457, 2017/10/27 2017.

[43] R.-J. Yu, Y.-L. Ying, R. Gao, and Y.-T. Long, "Confined Nanopipette Sensing: From Single Molecules, Single Nanoparticles, to Single Cells," *Angewandte Chemie International Edition,* vol. 58, pp. 3706-3714, 2019.

[44] X. Gong, A. V. Patil, A. P. Ivanov, Q. Kong, T. Gibb, F. Dogan, *et al.*, "Label-Free In-Flow Detection of Single DNA Molecules using Glass Nanopipettes," *Analytical Chemistry,* vol. 86, pp. 835-841, 2014/01/07 2014.

[45] S. Instruments. (2010). *P-2000 Laser Based Micropipette Puller System Operation Manual*. Available: www.sutter.com

[46] J. Stanley and N. Pourmand, "Nanopipettes—The past and the present," *APL Materials,* vol. 8, p. 100902, 2020.

[47] D. Perry, D. Momotenko, R. A. Lazenby, M. Kang, and P. R. Unwin, "Characterization of Nanopipettes," *Analytical Chemistry,* vol. 88, pp. 5523-5530, 2016/05/17 2016.

[48] P. Actis, A. C. Mak, and N. Pourmand, "Functionalized nanopipettes: toward label-free, single cell biosensors," *Bioanalytical Reviews,* vol. 1, pp. 177-185, 2010/08/01 2010.

[49] D. Sánchez, N. Johnson, C. Li, P. Novak, J. Rheinlaender, Y. Zhang, *et al.*, "Noncontact Measurement of the Local Mechanical Properties of Living Cells Using Pressure Applied via a Pipette," *Biophysical Journal,* vol. 95, pp. 3017-3027, 2008/09/15/ 2008.

[50] C. Wei, A. J. Bard, and S. W. Feldberg, "Current Rectification at Quartz Nanopipet Electrodes," *Analytical Chemistry,* vol. 69, pp. 4627-4633, 1997/11/01 1997.

[51] T. F. Fuller and J. N. Harb, *Electrochemical engineering,* 1st edition ed. Hoboken, New Jersey: Wiley, 2018.

[52] D. G. Haywood, A. Saha-Shah, L. A. Baker, and S. C. Jacobson, "Fundamental Studies of Nanofluidics: Nanopores, Nanochannels, and Nanopipets," *Analytical Chemistry,* vol. 87, pp. 172-187, 2015/01/06 2015.

[53] S. R. German, L. Luo, H. S. White, and T. L. Mega, "Controlling Nanoparticle Dynamics in Conical Nanopores," *The Journal of Physical Chemistry C,* vol. 117, pp. 703-711, 2013/01/10 2013.

[54] R. B. Schoch, J. Han, and P. Renaud, "Transport phenomena in nanofluidics," *Reviews of Modern Physics,* vol. 80, pp. 839-883, 07/17/ 2008.

[55] T. Uchikoshi, "Chapter 3.2.2.2. - Electrokinetic effects in liquid," in *Nanoparticle Technology Handbook (Second Edition)*, M. Hosokawa, K. Nogi, M. Naito, and T. Yokoyama, Eds., ed Amsterdam: Elsevier, 2012, pp. 113-176.

[56] Z. S. Siwy, "Ion-Current Rectification in Nanopores and Nanotubes with Broken Symmetry," *Advanced Functional Materials,* vol. 16, pp. 735-746, 2006.

[57] S. Klinge, F. Voigts-Hoffmann, M. Leibundgut, and N. Ban, "Atomic structures of the eukaryotic ribosome," *Trends Biochem Sci,* vol. 37, pp. 189-98, May 2012.

[58] B. Alberts, *Molecular biology of the cell*, Sixth edition. ed. New York, NY: Garland Science, Taylor and Francis Group, 2015.

[59] G. M. Cooper, *The cell : a molecular approach*, 2nd ed. ed. Washington, D.C: ASM Press, 2000.

[60] S. Clancy and W. Brown, "Translation: DNA to mRNA to protein," *Nature Education,* vol. 1, p. 101, 2008.

[61] Erin E. Heyer and Melissa J. Moore, "Redefining the Translational Status of 80S Monosomes," *Cell,* vol. 164, pp. 757-769, 2016/02/11/ 2016.

[62] J. R. Warner and P. M. Knopf, "The discovery of polyribosomes," *Trends in Biochemical Sciences,* vol. 27, pp. 376-380, 2002/07/01/ 2002.

[63] Z. A. Afonina and V. A. Shirokov, "Three-Dimensional Organization of Polyribosomes–A Modern Approach," *Biochemistry (Moscow),* vol. 83, pp. S48-S55, 2018/01/01 2018.

[64] Z. A. Afonina, A. G. Myasnikov, V. A. Shirokov, B. P. Klaholz, and A. S. Spirin, "Conformation transitions of eukaryotic polyribosomes during multi-round translation," *Nucleic Acids Research,* vol. 43, pp. 618-628, 2015.

[65] H. A. King and A. P. Gerber, "Translatome profiling: methods for genome-scale analysis of mRNA translation," *Briefings in Functional Genomics,* vol. 15, pp. 22-31, 2016.

[66] V. Au - Gandin, K. Au - Sikström, T. Au - Alain, M. Au - Morita, S. Au - McLaughlan, O. Au - Larsson, *et al.*, "Polysome Fractionation and Analysis of Mammalian Translatomes on a Genome-wide Scale," *JoVE,* p. e51455, 2014/05/17/ 2014.

[67] A. C. Panda, J. L. Martindale, and M. Gorospe, "Polysome Fractionation to Analyze mRNA Distribution Profiles," *Bio-protocol,* vol. 7, p. e2126, 2017.

[68] S. Liang, H. M. Bellato, J. Lorent, F. C. S. Lupinacci, C. Oertlin, V. van Hoef, *et al.*, "Polysome-profiling in small tissue samples," *Nucleic acids research,* vol. 46, pp. e3-e3, 2018.

[69] T. Mašek, L. Valášek, and M. Pospíšek, "Polysome Analysis and RNA Purification from Sucrose Gradients," in *RNA: Methods and Protocols,* H. Nielsen, Ed., ed Totowa, NJ: Humana Press, 2011, pp. 293-309.

[70] Y. Arava, Y. Wang, J. D. Storey, C. L. Liu, P. O. Brown, and D. Herschlag, "Genome-Wide Analysis of mRNA Translation Profiles in Saccharomyces cerevisiae," *Proceedings of the National Academy of Sciences - PNAS,* vol. 100, pp. 3889-3894, 2003.

[71] J. L. Aspden, Y. C. Eyre-Walker, R. J. Phillips, U. Amin, M. A. S. Mumtaz, M. Brocard, *et al.*, "Extensive translation of small Open Reading Frames revealed by Poly-Ribo-Seq," *eLife,* vol. 3, p. e03528, 2014/08/21 2014.

[72] H. Yoshikawa, M. Larance, D. J. Harney, R. Sundaramoorthy, T. Ly, T. Owen-Hughes, *et al.*, "Efficient analysis of mammalian polysomes in cells and tissues using Ribo Mega-SEC," *eLife,* vol. 7, p. e36530, 2018/08/10 2018.

[73] D. Simsek, G. C. Tiu, R. A. Flynn, G. W. Byeon, K. Leppek, A. F. Xu, *et al.*, "The Mammalian Ribo-interactome Reveals Ribosome Functional Diversity and Heterogeneity," *Cell*, vol. 169, pp. 1051-1065.e18, 2017.

[74] M. Wanunu, S. Bhattacharya, Y. Xie, Y. Tor, A. Aksimentiev, and M. Drndic, "Nanopore Analysis of Individual RNA/Antibiotic Complexes," *ACS Nano*, vol. 5, pp. 9345-9353, 2011/12/27 2011.

[75] Y. Astier, D. E. Kainov, H. Bayley, R. Tuma, and S. Howorka, "Stochastic Detection of Motor Protein–RNA Complexes by Single-Channel Current Recording," *ChemPhysChem*, vol. 8, pp. 2189-2194, 2007/10/22 2007.

[76] C. Shasha, R. Y. Henley, D. H. Stoloff, K. D. Rynearson, T. Hermann, and M. Wanunu, "Nanopore-Based Conformational Analysis of a Viral RNA Drug Target," *ACS Nano*, vol. 8, pp. 6425-6430, 2014/06/24 2014.

[77] A. M. Smith, R. Abu-Shumays, M. Akeson, and D. L. Bernick, "Capture, Unfolding, and Detection of Individual tRNA Molecules Using a Nanopore Device," *Frontiers in Bioengineering and Biotechnology*, vol. 3, 2015-June-24 2015.

[78] R. Y. Henley, B. A. Ashcroft, I. Farrell, B. S. Cooperman, S. M. Lindsay, and M. Wanunu, "Electrophoretic Deformation of Individual Transfer RNA Molecules Reveals Their Identity," *Nano Letters*, vol. 16, pp. 138-144, 2016/01/13 2016.

[79] X. Zhang, D. Zhang, C. Zhao, K. Tian, R. Shi, X. Du, *et al.*, "Nanopore electric snapshots of an RNA tertiary folding pathway," *Nature Communications*, vol. 8, p. 1458, 2017/11/13 2017.

[80] M. Rahman, M. A. Stott, M. Harrington, Y. Li, M. J. N. Sampad, L. Lancaster, *et al.*, "On demand delivery and analysis of single molecules on a programmable nanopore-optofluidic device," *Nature Communications*, vol. 10, p. 3712, 2019/08/16 2019.

[81] M. Raveendran, A. R. Leach, T. Hopes, J. L. Aspden, and P. Actis, "Ribosome Fingerprinting with a Solid-State Nanopore," *ACS Sensors*, 2020/10/28 2020.

[82] C. C. Chau, S. E. Radford, E. W. Hewitt, and P. Actis, "Macromolecular Crowding Enhances the Detection of DNA and Proteins by a Solid-State Nanopore," *Nano Letters*, vol. 20, pp. 5553-5561, 2020/07/08 2020.

[83] A. Balijepalli, J. W. F. Robertson, J. E. Reiner, J. J. Kasianowicz, and R. W. Pastor, "Theory of Polymer–Nanopore Interactions Refined Using Molecular Dynamics Simulations," *Journal of the American Chemical Society*, vol. 135, pp. 7064-7072, 2013/05/08 2013.

[84] N. Meyer, N. Arroyo, J.-M. Janot, M. Lepoitevin, A. Stevenson, I. A. Nemeir, *et al.*, "Detection of Amyloid-β Fibrils Using Track-Etched Nanopores: Effect of Geometry and Crowding," *ACS Sensors*, vol. 6, pp. 3733-3743, 2021/10/22 2021.

[85] L. Meertens, M. L. Hafirassou, T. Couderc, L. Bonnet-Madin, V. Kril, B. M. Kümmerer, *et al.*, "FHL1 is a major host factor for chikungunya virus infection," *Nature*, vol. 574, pp. 259-263, 2019/10/01 2019.

[86] A. Cann, *Principles of molecular virology*, Fifth edition. ed. London: Academic, 2011.

[87] S. Khongwichit, J. Chansaenroj, C. Chirathaworn, and Y. Poovorawan, "Chikungunya virus infection: molecular biology, clinical characteristics, and epidemiology in Asian countries," *Journal of Biomedical Science*, vol. 28, p. 84, 2021/12/02 2021.

[88] E. Hoornweg Tabitha, K. S. van Duijl-Richter Mareike, V. Ayala Nuñez Nilda, C. Albulescu Irina, J. van Hemert Martijn, and M. Smit Jolanda, "Dynamics of Chikungunya Virus Cell Entry Unraveled by Single-Virus Tracking in Living Cells," *Journal of Virology*, vol. 90, pp. 4745-4756, 2016.

[89] S. K. Singh and S. K. Unni, "Chikungunya virus: host pathogen interaction," *Reviews in Medical Virology*, vol. 21, pp. 78-88, 2011.

[90] R. Remenyi, Y. Gao, R. E. Hughes, A. Curd, C. Zothner, M. Peckham, *et al.*, "Persistent Replication of a Chikungunya Virus Replicon in Human Cells Is

Associated with Presence of Stable Cytoplasmic Granules Containing Nonstructural Protein 3," *Journal of Virology,* vol. 92, pp. e00477-18, 2018.

[91] E. A. Madden, K. S. Plante, C. R. Morrison, K. M. Kutchko, W. Sanders, K. M. Long, *et al.*, "Using SHAPE-MaP To Model RNA Secondary Structure and Identify 3′UTR Variation in Chikungunya Virus," *Journal of Virology,* vol. 94, pp. e00701-20, 2020.

[92] M. K. S. van Duijl-Richter, J. S. Blijleven, A. M. van Oijen, and J. M. Smit, "Chikungunya virus fusion properties elucidated by single-particle and bulk approaches," *Journal of General Virology,* vol. 96, pp. 2122-2132, 2015.

[93] P. Novak, C. Li, A. I. Shevchuk, R. Stepanyan, M. Caldwell, S. Hughes, *et al.*, "Nanoscale live-cell imaging using hopping probe ion conductance microscopy," *Nature Methods,* vol. 6, p. 279, 03/01/online 2009.

[94] J. Rheinlaender, N. A. Geisse, R. Proksch, and T. E. Schäffer, "Comparison of Scanning Ion Conductance Microscopy with Atomic Force Microscopy for Cell Imaging," *Langmuir,* vol. 27, pp. 697-704, 2011/01/18 2011.

[95] P. Actis, M. M. Maalouf, H. J. Kim, A. Lohith, B. Vilozny, R. A. Seger, *et al.*, "Compartmental Genomics in Living Cells Revealed by Single-Cell Nanobiopsy," *ACS Nano,* vol. 8, pp. 546-553, 2014/01/28 2014.

[96] R. Adam Seger, P. Actis, C. Penfold, M. Maalouf, B. Vilozny, and N. Pourmand, "Voltage controlled nano-injection system for single-cell surgery," *Nanoscale,* vol. 4, pp. 5843-5846, 2012.

[97] R. W. DeBlois and R. K. Wesley, "Sizes and concentrations of several type C oncornaviruses and bacteriophage T2 by the resistive-pulse technique," *Journal of Virology,* vol. 23, pp. 227-233, 1977/08/01 1977.

[98] K. Zhou, L. Li, Z. Tan, A. Zlotnick, and S. C. Jacobson, "Characterization of Hepatitis B Virus Capsids by Resistive-Pulse Sensing," *Journal of the American Chemical Society,* vol. 133, pp. 1618-1621, 2011/02/16 2011.

[99] H. Wu, Y. Chen, Q. Zhou, R. Wang, B. Xia, D. Ma, *et al.*, "Translocation of Rigid Rod-Shaped Virus through Various Solid-State Nanopores," *Analytical Chemistry,* vol. 88, pp. 2502-2510, 2016/02/16 2016.

[100] A. McMullen, H. W. de Haan, J. X. Tang, and D. Stein, "Stiff filamentous virus translocations through solid-state nanopores," *Nature Communications,* vol. 5, p. 4171, 2014/06/16 2014.

[101] P. Shabram and E. Aguilar-Cordova, "Multiplicity of Infection/Multiplicity of Confusion," *Molecular Therapy,* vol. 2, pp. 420-421, 2000.

[102] C. Nyberg-Hoffman, P. Shabram, W. Li, D. Giroux, and E. Aguilar-Cordova, "Sensitivity and reproducibility in adenoviral infectious titer determination," *Nat Med,* vol. 3, pp. 808-11, Jul 1997.

[103] A. Varble, R. A. Albrecht, S. Backes, M. Crumiller, N. M. Bouvier, D. Sachs, *et al.*, "Influenza A virus transmission bottlenecks are defined by infection route and recipient host," *Cell Host Microbe,* vol. 16, pp. 691-700, Nov 12 2014.

[104] A. B. Russell, C. Trapnell, and J. D. Bloom, "Extreme heterogeneity of influenza virus infection in single cells," *Elife,* vol. 7, Feb 16 2018.

[105] R. Schubert, S. Trenholm, K. Balint, G. Kosche, C. S. Cowan, M. A. Mohr, *et al.*, "Virus stamping for targeted single-cell infection in vitro and in vivo," *Nature Biotechnology,* vol. 36, pp. 81-88, 2018/01/01 2018.

[106] P. Stiefel, F. I. Schmidt, P. Dörig, P. Behr, T. Zambelli, J. A. Vorholt, *et al.*, "Cooperative Vaccinia Infection Demonstrated at the Single-Cell Level Using FluidFM," *Nano Letters,* vol. 12, pp. 4219-4227, 2012/08/08 2012.

[107] Krishnamoorthy, S. ed., 2017. *Nanomaterials: A guide to fabrication and applications.* CRC Press.

[108] O. Guillaume-Gentil, E. Potthoff, D. Ossola, C. M. Franz, T. Zambelli, and J. A. Vorholt, "Force-controlled manipulation of single cells: from AFM to FluidFM," *Trends in Biotechnology,* vol. 32, pp. 381-388, 2014/07/01/ 2014.

[109] N. R. Genuth and M. Barna, "The Discovery of Ribosome Heterogeneity and Its Implications for Gene Regulation and Organismal Life," *Molecular Cell,* vol. 71, pp. 364-374, 2018.

[110] Y.-H. Shiao, "Promising Assays for Examining a Putative Role of Ribosomal Heterogeneity in COVID-19 Susceptibility and Severity," *Life,* vol. 12, p. 203, 2022.

[111] C. C. Chau, F. Marcuccio, D. Soulias, M. A. Edwards, S. E. Radford, E. W. Hewitt, *et al.,* "Cooperative electrolyte-PEG interactions drive the signal amplification in a solid-state nanopore," *bioRxiv,* p. 2021.11.01.466478, 2021.

[112] S. W. Kowalczyk, D. B. Wells, A. Aksimentiev, and C. Dekker, "Slowing down DNA Translocation through a Nanopore in Lithium Chloride," *Nano Letters,* vol. 12, pp. 1038-1044, 2012/02/08 2012.

[113] Z.-X. Wei, Y.-L. Ying, M.-Y. Li, J. Yang, J.-L. Zhou, H.-F. Wang, *et al.,* "Learning Shapelets for Improving Single-Molecule Nanopore Sensing," *Analytical Chemistry,* vol. 91, pp. 10033-10039, 2019/08/06 2019.

[114] A. P. Ivanov, P. Actis, P. Jönsson, D. Klenerman, Y. Korchev, and J. B. Edel, "On-Demand Delivery of Single DNA Molecules Using Nanopipets," *ACS Nano,* vol. 9, pp. 3587-3595, 2015/04/28 2015.